NASA TECHNICAL NOTE

NASA TN D-7045

A MATHEMATICAL PROCEDURE FOR PREDICTING THE TOUCHDOWN DYNAMICS OF A SOFT-LANDING VEHICLE

by George A. Zupp, Jr., and Harold H. Doiron

Manned Spacecraft Center
Houston, Texas 77058

1. Report No. NASA TN D-7045	2. Government Accession No.	3. Recipient's Catalog No.	
4. Title and Subtitle A MATHEMATICAL PROCEDURE FOR PREDICTING THE TOUCHDOWN DYNAMICS OF A SOFT-LANDING VEHICLE		5. Report Date February 1971	
		6. Performing Organization Code	
7. Author(s) George A. Zupp, Jr., and Harold H. Doiron, MSC		8. Performing Organization Report No. MSC S-241	
		10. Work Unit No. 914-50-20-89-72	
9. Performing Organization Name and Address Manned Spacecraft Center Houston, Texas 77058		11. Contract or Grant No.	
		13. Type of Report and Period Covered Technical Note	
12. Sponsoring Agency Name and Address National Aeronautics and Space Administration Washington, D.C. 20546		14. Sponsoring Agency Code	

15. Supplementary Notes

16. Abstract

A mathematical procedure for simulating the touchdown dynamics of a soft-landing spacecraft is presented. The mathematical model considers the spacecraft to be a rigid body with six degrees of freedom to which several telescoping leg-type landing gears are attached. Sufficient generality is provided to account for effects from the following: strut stroking, bending, and binding; the reaction control system; descent engine thrust tailoff; descent engine nozzle crushing; and various landing-surface/landing-gear-footpad interactions. The analysis, which has been used extensively in the study of lunar module landing dynamics, is compared to experimental data from drop tests of a 1/6-scale lunar module model.

17. Key Words (Suggested by Author(s)) · Digital Simulation · Lunar Module · Touchdown Dynamics · Landing Stability	18. Distribution Statement Unclassified - Unlimited		
19. Security Classif. (of this report) None	20. Security Classif. (of this page) None	21. No. of Pages 85	22. Price* $3.00

CONTENTS

TABLE

FIGURES

A MATHEMATICAL PROCEDURE FOR PREDICTING THE TOUCHDOWN

DYNAMICS OF A SOFT-LANDING VEHICLE

By George A. Zupp, Jr., and Harold H. Doiron
Manned Spacecraft Center

SUMMARY

A mathematical procedure for predicting the touchdown dynamics of a soft-landing vehicle is presented. The vehicle is idealized as a pseudorigid structure to which a landing gear system is attached. The landing gear system is made up of telescoping struts which house shock-absorbing mechanisms and connect the vehicle structure with footpads that contact the landing surface. The forces acting on the idealized vehicle during landing are from the vehicle landing gear system, the reaction control system, the descent-stage rocket engine thrust, rocket-engine-nozzle-crushing loads, and gravity. Forces acting on footpads are due to forces from the landing gear struts and from the landing surface. The elastic properties of the vehicle structure and of the landing gear system are approximated by assuming that the structure deforms linearly with the applied load. Correlation between analytical and experimental data is presented for a 1/6-scale lunar module model. Conclusions from these data are presented.

INTRODUCTION

A primary objective of the Apollo Program is to soft-land a manned spacecraft, the lunar module (LM), on the lunar surface. During the first critical seconds of touchdown, the landing gear system must absorb the kinetic and potential energies of the spacecraft without causing the LM to topple and must attenuate the landing loads to preclude damage to the spacecraft structure or possible injury to the astronauts. To ensure that the landing gear system has the capability to arrest the spacecraft motion safely, landing gear performance must be established. Although methods of determining landing gear performance for aircraft systems are well established, these methods are not directly applicable to spacecraft, primarily because of the differences in configurations. Consequently, development of new analytical and experimental procedures has been necessary to determine LM landing performance, as well as to aid in the development of the landing gear system. One of the more elaborate analytical procedures that has been developed for simulation of touchdown dynamics and for landing gear development is discussed in this report. Although developed for the LM, the procedure is applicable to other soft-landing spacecraft.

In the initial development phase of the Apollo LM landing gear system, analytical simulations of touchdown dynamics by a NASA contractor (ref. 1) and by the NASA

Manned Spacecraft Center (MSC) (ref. 2) were primarily restricted to landings on rigid surfaces that resulted in planar motion. These types of landings were considered critical for vehicle stability and landing gear energy absorption. Analysis of the touchdown dynamics of rigid models at the NASA Langley Research Center (refs. 3 and 4) indicated that, from a stability standpoint, nonplanar landings could be more severe than planar landings. As a result of this finding, more emphasis was placed on the simulation of nonplanar landings for LM touchdown analysis; consequently, the touchdown analysis presented in this paper evolved.

The purpose of this report is twofold:

1. To document the analytical procedures used in developing a mathematical model in the LM lunar landing dynamics

2. To make these procedures available to others who may be confronted with the task of mathematically modeling the touchdown dynamics of a soft-landing vehicle

This report includes a definition of pertinent coordinate systems and coordinate transformations. The equations of motion governing both rigid-vehicle and landing-gear-footpad dynamics are presented, together with the numerical procedure employed to solve the equations. Considerable detail is provided in defining the kinematic relationships used to model the articulating landing gear geometry. Various forces generated in the landing gear struts and the manner in which these forces are computed are discussed. A general description of the techniques used to model a reaction control system (RCS), descent engine rocket thrust, and descent engine nozzle crushing is also provided. Both rigid and nonrigid landing surface models are discussed, and considerable detail is provided on the manner in which various surface irregularities and footpad constraints are simulated. Data from the digital simulation analysis and a 1/6-scale LM model drop-test program are compared, and conclusions regarding the accuracy of the simulation technique are made.

The authors are particularly indebted to Joseph A. Reid, formerly of ITT Federal Electric Corp., for his efforts in the assembly and preparation of this report. The authors also wish to express sincere appreciation to John A. Schliesing and Ben W. Holder, MSC, for their technical comments and suggestions.

SYMBOLS

AMP	amplification factor for the descent propulsion system rocket thrust due to the nozzle exit plane approaching the landing surface
AP	area of the bottom of a footpad, in^2
APF	frontal area of a footpad in contact with soil, in^2

$\vec{A}_{n,j}$ — instantaneous vector directed from the nth footpad center to a fixed point on the jth surface curb

$\vec{AB}$ — vector directed from footpad A to footpad B

$\vec{ACM}$ — vector connecting the rigid-vehicle center of mass and a landing gear footpad

$\hat{AI}_{n,j}$ — unit vector normal to the jth surface curb and directed from the initial surface contact point of the nth footpad

$a_{n,j} = DWALLI_{n,j} \cos WALANG_{n,j}$

$\vec{B1}_n$ — vector directed from the origin of the body coordinate system to the primary-to-secondary-strut attachment point of the nth landing gear assembly

$\vec{B2}_n, \vec{B3}_n, \vec{B4}_n$ — vectors directed from the origin of the body coordinate system to the rigid-structure attachment points of the primary and secondary struts in the nth landing gear assembly

$\hat{B}_{n,j}$ — unit vector directed along the jth surface curb of the nth footpad

$\vec{BP}_n$ — vector directed from the origin of the body coordinate system to the footpad of the nth landing gear assembly

$b_{n,j} = DWALLI_{n,j} \sin WALANG_{n,j}$

$CLUEW_n$ — computer program input clue used to define the curbs on the landing surface for the nth footpad

CP — constant used to compute primary strut stroking-velocity-dependent force, $(lb/(ft/sec))^{\gamma_p}$

CS — constant used to compute secondary strut stroking-velocity-dependent force, $(lb/(ft/sec))^{\gamma_s}$

$C\theta_x, C\theta_y, C\theta_z$ — commanded values for the Euler angles used in the RCS simulation, deg

$C\omega_x, C\omega_y, C\omega_z$ — commanded attitude rates used in the RCS simulation, deg/sec

c	constant used in numerical integration (eq. (20)), ft/sec^3
$D1_n$	length of the nth primary strut inner cylinder, ft
$D2_n$	initial bearing separation in the nth primary strut, ft
DIST	desired maximum allowable movement per integration step between the footpads and the rigid-vehicle center of mass, ft
$DWALL_{n,j}$	instantaneous distance between the nth footpad center and the jth constraining curb, ft
$DWALLI_{n,j}$	normal distance between the nth footpad center and the jth curb when the footpad initially contacts the surface, ft
$D\theta_x, D\theta_y, D\theta_z$	deviations in Euler angles from the commanded values, deg
EI	constant bending stiffness of a primary strut, $lb\text{-}ft^2$
EX, EY, EZ	combined attitude and attitude rate errors used in RCS simulation
EXM, EYM, EZM	deadband widths for RCS simulation
$E\theta_x, E\theta_y, E\theta_z$	attitude errors for the body axes used in RCS simulation, deg
$E\omega_x, E\omega_y, E\omega_z$	attitude rate errors used in RCS simulation, deg/sec
F_1	magnitude of descent engine thrust at touchdown, lb
$F_{B,x}, F_{B,y}, F_{B,z}$	components of sloshing force vector (eq. (115)), lb
F_s	force per unit vertical tank acceleration caused by a unit sloshing amplitude, $(lb/ft)/(ft/sec^2)$
F_w	total force applied to the tank wall by the sloshing propellant, lb
$F1_n$	force at bearing 1 of the primary strut (fig. 14), lb
$F2_n$	force at bearing 2 of the primary strut (fig. 14), lb

$F31_n$, $F41_n$	instantaneous axial force in the secondary struts of the nth landing gear assembly, lb
FBR	friction forces present during strut stroking, lb
FBR_n	primary strut bearing friction force in the nth primary strut, lb
$FC31_n$, $FC41_n$	secondary strut stroke-dependent forces in the nth landing gear assembly, lb
FCP_n	stroke-dependent force in the nth primary strut, lb
FP1, FP2	first- and second-stage crushing forces of the honeycomb shock absorbers in the primary struts, lb
FRCSZ	Z-component of $\overrightarrow{FRCS}$, lb
FSC1, FSC2	compression stroking forces of the secondary struts for the first- and second-stage honeycomb cartridges, lb
FST1, FST2	tension stroking forces of the secondary struts for the first- and second-stage honeycomb cartridges, lb
$FV31_n$, $FV41_n$	stroking-velocity-dependent forces in the nth landing gear secondary struts, lb
FVP	viscous forces present during strut stroking, lb
FVP_n	stroking-velocity-dependent force in the nth landing gear primary strut, lb
FX, FY, FZ	forces on the idealized rigid vehicle resolved along the X-, Y-, and Z-axes, respectively, lb
FXP_n, FYP_n, FZP_n	forces on the nth footpad in the X-, Y-, and Z-directions, which are independent of the instantaneous sliding direction of the footpad, lb
FZI_n	force component normal to the landing surface applied to the nth footpad by the landing gear, lb

$\vec{F}$ | total force vector acting on the idealized-vehicle center of mass

$\vec{F}_{TF}$ | total force vector due to engine thrust and the nozzle failing load

$\overrightarrow{F2P}_n$ | instantaneous axial force in the primary strut inner cylinder of the nth landing gear assembly, produced by compression stroking of the primary strut

$\overrightarrow{FCMG}$ | total landing gear forces acting on the vehicle center of mass expressed in the inertial coordinate system

$\overrightarrow{FDRAG}_n$ | soil drag force acting on the nth footpad

$\overrightarrow{FDRAGP}_n$ | frictional drag force on the bottom of the nth footpad

$\overrightarrow{FFL}$ | nozzle failure load vector

$\overrightarrow{FGRND}_n$ | drag force on the nth footpad with direction opposite to the instantaneous sliding direction of the footpad in the X-Y plane

$\overrightarrow{FM}_n$ | force normal to the primary strut at the nth footpad

$\overrightarrow{FN}_n$ | component of the secondary strut forces normal to the nth primary strut

$\overrightarrow{FP}_n$ | resultant force on the nth footpad due to landing gear forces

$\overrightarrow{FPI}_n$ | resultant of the nth landing gear forces acting on the rigid-vehicle center of mass, expressed in the inertial coordinate system

$\overrightarrow{FRCS}$ | net force vector produced by the RCS jets

$\overrightarrow{FRCSI}$ | RCS jet force in the inertial coordinate system

$\overrightarrow{FS}_n$ | vector sum of the secondary strut forces acting on the nth primary strut

$\overrightarrow{FTFI}$ | force vector on the rigid-vehicle center of mass due to engine thrust and nozzle failing load, expressed in the inertial coordinate system

$\overrightarrow{\text{FTHRUST}}$ — thrust force of the descent propulsion system rocket

$\overrightarrow{\text{FWF}}_{n,j}$ — friction force between the nth footpad and the jth surface curb

$\overrightarrow{\text{FXYP}}_n$ — force vector on the nth footpad independent of the instantaneous sliding direction of the footpad

GOXX, -GOXY, GOXZ, GOYX, -GOYY, -GOYZ, -GOZX, GOZY, GOZZ — components of the body coordinate system to inertial coordinate system transformation matrix (eq. (2))

$\vec{\text{G}}$ — gravitational acceleration vector expressed in inertial coordinates

g_x, g_y, g_z — components of the gravitational acceleration vector expressed in the inertial coordinate system along the X-, Y-, and Z-axes, respectively, ft/sec^2

HOLE_n — parameter which defines the surface elevation for the nth footpad, ft

I_{xx}, I_{yy}, I_{zz} — mass moments of inertia about the X_B-, Y_B-, and Z_B-axes, respectively, $slug$-ft^2

$I_{xx,f}, I_{yy,f}, I_{zz,f}$ — modified mass moments of inertia in the body coordinate system of the rigid vehicle, corrected for exclusion of the sloshing mass, $slug$-ft^2

I_{xy} — cross product of inertia with respect to the X_B-Y_B plane, $slug$-ft^2

I_{xz} — cross product of inertia with respect to the X_B-Z_B plane, $slug$-ft^2

I_{yz} — cross product of inertia with respect to the Y_B-Z_B plane, $slug$-ft^2

i, j, k, n — indices

K — constant characterizing the thrust tailoff properties, 1/sec

K_1 — bearing strength of the soil at the surface, psi

K_2 — increase in soil bearing strength with depth, psi/ft

K_3	increase in soil bearing strength with footpad velocity, psi/(ft/sec)
K_4	increase in soil bearing strength with the square of the footpad velocity, psi/(ft/sec)^2
K_5	static soil resistance to horizontal movement, psi
K_6	increase in soil resistance to horizontal motion with respect to footpad lateral displacement, psi/ft
K_7	increase in lateral resistance of the soil with respect to the depth of penetration of the footpad, psi/ft
K_8	increase in soil resistance with respect to the square of the footpad horizontal velocity, psi/(ft/sec)^2
K_H	spring constant representative of the elastic property of the honeycomb shock-absorber material, lb/ft
$K_{P,B}$	primary strut backoff spring rate without trunnion-point elasticity, lb/ft
$K_{P,o}$	primary strut onset spring rate without trunnion-point elasticity, lb/ft
K_S	spring constant representative of the slope of the load-deflection curve of the spacecraft structure at a trunnion point, lb/ft
$K_{SC,B}$	secondary strut backoff spring rate in compression stroking without trunnion-point elasticity, lb/ft
$K_{SC,o}$	secondary strut onset spring rate in compression stroking without trunnion-point elasticity, lb/ft
$K_{ST,B}$	secondary strut backoff spring rate in tension stroking without trunnion-point elasticity, lb/ft
$K_{ST,o}$	secondary strut onset spring rate in tension stroking without trunnion-point elasticity, lb/ft
K_{TP}	trunnion-point spring rate at the primary strut-structure attachment point, lb/ft
K_{TS}	trunnion-point spring rate at the secondary strut-structure attachment point, lb/ft

$K'_{P,B}$	modified backoff compression spring rate for the primary struts, lb/ft
$K'_{P,o}$	modified onset compression spring rate for the primary struts, lb/ft
$K'_{SC,B}$	modified backoff compression spring rate for the secondary struts, lb/ft
$K'_{SC,o}$	modified onset compression spring rate for the secondary struts, lb/ft
$K'_{ST,B}$	modified backoff tension spring rate for the secondary struts, lb/ft
$K'_{ST,o}$	modified onset tension spring rate for the secondary struts, lb/ft
$KB3_n, KB4_n$	spring rates for secondary struts as a result of primary strut bending, lb/ft
$k_{11}, k_{12}, k_{21}, k_{22}, k_{31}, k_{32}$	constants which model a given RCS control mode
$L21_n$	distance along the nth primary strut from the upper attachment point to the secondary strut attachment point, ft
$L31_n, L41_n, L2P_n$	undeformed lengths of the secondary and primary struts of the nth landing gear assembly, ft
ℓ	any given distance below the quiescent propellant surface (fig. 28), ft
ℓ_1	distance from the spacecraft center of mass to the plane of the quiescent propellant surface (fig. 29), ft
ℓ_2	distance from the spacecraft center of mass with propellant to the spacecraft center of mass without propellant (fig. 29), ft
M	mass of the idealized rigid vehicle, slugs
M_0, M_1, M_2	constants characterizing the rocket engine thrust tailoff properties
M_f	fixed mass of residue propellant, slugs
M_S	sloshing mass of residue propellant, slugs

$M(s)$	bending moment as a function of length along the primary strut, ft-lb
$\overrightarrow{MRCS}$	RCS torque vector
$\overrightarrow{MS}_n$	moment vector perpendicular to the nth primary strut, caused by action of secondary struts
$\overrightarrow{MTF}$	moment vector acting on the idealized vehicle due to the rocket thrust and nozzle failure load
m	number of landing gears
$OBST_n$	parameter which defines the height of constraining obstacles for the nth footpad, ft
P_n	point where the primary strut is joined to the nth footpad
$PFRC_{n,j}$	crushing force of the nth footpad against the jth surface curb, lb
$PMASS$	effective mass of each footpad, slugs
PR	undeformed footpad radius, ft
$PSTRK_{n,j}$	variable indicating the amount of nth footpad crushing normal to the jth curb, ft
q	sloshing amplitude, ft
$\ddot{q}_B$	rigid-vehicle acceleration of the propellant tank normal to the vertical axis of the tank, ft/sec^2
$R1, R2, R3$	distances from the center line of the LM defining the landing gear geometry (fig. 23), ft
$\overrightarrow{R}_F$	vector from the origin of the body coordinate system to the centroid of the nozzle failure load
$\overrightarrow{R}_T$	vector from the origin of the body coordinate system to the centroid of the nozzle exit plane
$S2P_n$	compression stroke of the nth primary strut, ft
$S31_n, S41_n$	stroke of the secondary struts in the nth landing gear assembly, ft

SP_n	lateral translation of a footpad, ft
$\overrightarrow{SD}$	vector directed from the rigid-vehicle center of mass normal to a vertical plane through two adjacent footpads
s	position coordinate along the length of the primary strut, ft
$\left[T_{BE}\right]$	transformation used to transform body angular rates to Euler angular rates
$\left[T_{BI}\right]$	transformation used to transform vector components from body system coordinates to inertial system coordinates
$\left[T_{EB}\right]$	transformation used to transform Euler angular rates to body angular rates
$\left[T_{GI}\right]$	transformation used to transform vector components from gravity system coordinates to inertial system coordinates
$\left[T_{IB}\right]$	transformation used to transform vector components in the inertial system coordinates to the body system coordinates
$\left[T_{IG}\right]$	transformation used to transform vector components from inertial system coordinates to gravity system coordinates
$T_{f,x}, T_{f,y}$	torques about the X_B- and Y_B-axes, respectively, due to propellant sloshing, ft-lb
T_x, T_y, T_z	resultant torques about the X_B-, Y_B-, and Z_B-axes, respectively, ft-lb
TORQX	magnitude of the torque generated about the X_B-axis by RCS thrusters, ft-lb
TRCSX, TRCSY, TRCSZ	RCS torques about the X_B-, Y_B-, and Z_B-axes, respectively, ft-lb
$\overrightarrow{T}$	net torque about the idealized-vehicle center of mass
$\overrightarrow{TAF}$	total engine thrust force, the product of the amplification factor AMP and the normal thrust force $\overrightarrow{FTHRUST}$
$\overrightarrow{TCMG}$	resultant torque about the rigid-vehicle center of mass due to landing gear strut loads
t	time, sec

t_1	time of LM descent engine thrust termination command, sec
t_2	time at which descent engine thrust starts to tailoff, sec
t_k	time at the beginning of the kth integration step, sec
t_o	reference start time for engine thrust tailoff curve, sec
t_p	time at which the LM footpad touches the surface, sec
U_n	coefficient of sliding friction between the nth footpad and the landing surface
UW_n	coefficient of friction between the nth footpad and surface curbs
V_h	horizontal touchdown velocity, ft/sec
V_o	overturning velocity, which is a measure of the degree of instability of an unstable landing, ft/sec
V_v	vertical touchdown velocity, ft/sec
VEL	absolute value of the maximum relative velocity between the rigid-vehicle center of mass and the landing gear footpads, ft/sec
$\vec{V}$	translation velocity vector of the rigid-vehicle center of mass
$\overrightarrow{V21}_n$	vector directed along the center line of the nth primary strut from the upper end of the strut to the secondary strut attachment point
$\overrightarrow{V2P}_n, \overrightarrow{V31}_n, \overrightarrow{V41}_n$	vectors defining the instantaneous strut geometry of the nth landing gear assembly (fig. 5(b))
$\overrightarrow{W}_{n,j}$	position vector locating the intersection point of $DWALLI_{n,j}$ with a curb
$WALANG_{n,j}$	angle from the positive X-axis to a line in the X-Y plane normal to a curb, deg
X, Y, Z	inertial coordinate system axes

X_B, Y_B, Z_B	body coordinate system axes
X_G, Y_G, Z_G	gravity coordinate system axes
$XB4_n, YB4_n, ZB4_n, XB3_n,$ $YB3_n, ZB3_n, XB2_n, YB2_n,$ $ZB2_n, XB1_n, YB1_n, ZB1_n,$ XBP_n, YBP_n, ZBP_n	X_B, Y_B, and Z_B coordinates of several points defining landing gear geometry (eq. (26))
XP_n, YP_n, ZP_n	instantaneous position coordinates of the nth footpad in the inertial coordinate system, ft
XPI_n, YPI_n, ZPI_n	inertial coordinates of the nth footpad when it first contacts the landing surface, ft
$Z1, Z2, Z3, ZC$	spacecraft geometrical parameters, ft
$ZNOZ$	surface clearance of the centroid of the rocket-engine-nozzle exit plane, ft
$ZPEN_n$	vertical penetration of the nth landing gear footpad, ft
α	slope of the landing surface, deg
β	angle defining secondary strut geometry (fig. 23(b)), deg
γ_p, γ_s	exponents of the primary and secondary strut stroking velocities used to compute stroking-velocity-dependent forces
Δt	numerical integration step size, sec
$\delta_{3,n}, \delta_{4,n}$	bending deflections of the primary strut due to secondary strut loading, ft
δ_C	deflection of a secondary strut trunnion point due to compression loads (fig. 11(b)), ft
$\delta_{i,n}$	apparent change in length of the ith secondary strut due to n^{th} primary strut bending, ft
δ_P	deflection of the primary strut trunnion point (fig. 11(a)), ft
δ_T	deflection of a secondary strut trunnion point due to tension loads (fig. 11(b)), ft

η	bending deflection of the center line of an idealized primary strut, ft
η_n	bending deflection of the nth primary strut at the secondary-to-primary-strut attachment point due to strut loading, ft
$\theta_x, \theta_y, \theta_z$	Euler angles, deg
μ_B	primary strut bearing friction coefficient
ω_n	natural sloshing frequency, rad/sec
$\omega_x, \omega_y, \omega_z$	angular rate vector components of the rigid vehicle, expressed in the body coordinate system, deg/sec
ω^2	sloshing frequency squared per unit vertical tank acceleration (eq. (109)), $(\text{rad/sec}^2)/(\text{ft/sec}^2)$

Operators:

$(\dot{\ })$	first derivative with respect to time
$(\ddot{\ })$	second derivative with respect to time
$(\vec{\ })$	vector quantity
$(\dot{\vec{\ }})$	first derivative of a vector with respect to time
$(\ddot{\vec{\ }})$	second derivative of a vector with respect to time
$(\hat{\ })$	unit vector
$[\ ]$	matrix
$[\ ]^{-1}$	matrix inverse
$[\ ]^T$	matrix or column vector transpose

Symbols that represent vectors are also used without the vector notation in this paper; omission of the vector notation indicates absolute value of the vector.

GENERAL DISCUSSION OF THE MATHEMATICAL MODEL

The formulation of the mathematical model for predicting touchdown dynamics of a soft-landing system starts with the definition of the governing dynamics equations. In this case, the soft-lander cab is given three degrees of freedom in translation and three degrees of freedom in rotation. Each landing gear footpad is allowed three degrees of freedom in translation. The governing dynamics equations are the well-known Euler's equations for rotation and Newton's equations for translation. A numerical integration technique is employed to obtain the solution of these dynamics equations.

The significant forces acting on the idealized soft-landing vehicle are assumed to be those from the landing gear struts, the thrusting rocket engine, the RCS, the collapsing rocket engine nozzle, and gravity. The forces acting on the idealized footpads are due to surface-footpad interaction and forces from the landing gear struts. Propellant sloshing forces are also usually present during touchdown. When the propellant sloshing masses are small, the sloshing forces are considered to be negligible, and the propellant mass is treated as a rigid part of the vehicle structure. (In the appendix, a linear sloshing model is developed.) Care must be exercised in the application of linear sloshing models to touchdown dynamics problems because of the large sloshing amplitudes experienced during some touchdown conditions.

The landing gear is idealized as an arrangement of tubular struts with telescoping members, and the strut forces are assumed to be a function of Coulomb friction, strut stroke, and strut stroking rate. The landing gear and vehicle structural elasticity is approximated by the analogy that the structure deforms linearly with an applied load. However, the present model has been adapted for use with a more complex dynamic elastic model of the spacecraft structure which is described in reference 5.

The RCS and engine thrusting forces are guidance and control parameters and are functions of the landing procedure. A general discussion of the methods by which these forces are modeled is included.

Forces on the footpads result from landing gear strut forces and from resisting forces generated by the landing surface. Various landing surface models are discussed. In the early stages of the Apollo Program, the uncertainty of the composition of the lunar surface, from a bearing capacity standpoint, resulted in considerable work by a NASA contractor to define realistic soil surface models. The soil models developed by this contractor were incorporated into the mathematical touchdown simulation described in this report and were used to evaluate footpad penetrations for LM landings on postulated lunar surfaces (ref. 6). The soil model discussed in this report is a general model that allows the prediction of soil-footpad forces as a function of footpad movement and velocity. A rigid landing surface is also considered where the footpad is constrained upon surface contact or is allowed to slide under the influence of friction and constraining curbs.

COORDINATE SYSTEMS AND TRANSFORMATIONS

Three basic coordinate systems are used in the formulation of the mathematical simulation of the touchdown dynamics. Each coordinate system is an orthogonal right-hand system.

Inertial Coordinate System (X-, Y-, and Z-Axes)

The inertial coordinate system is defined such that the X-Y plane forms the landing surface. The Z-axis is perpendicular to and directed up from the X-Y plane. All of the rigid-vehicle and landing-gear-footpad equations of motion are expressed in the inertial coordinate system.

Gravity Coordinate System (X_G-, Y_G-, and Z_G-Axes)

In the gravity coordinate system, the negative Z_G-axis coincides with the gravity vector, and the X_G-axis coincides with the inertial system X-axis. The inertial system and the gravity system are related as shown in figure 1. The angle α between the Y_G- and Y-axes is the slope of the landing surface. The coordinate transformation $[T_{IG}]$ from the inertial system to the gravity system is given by
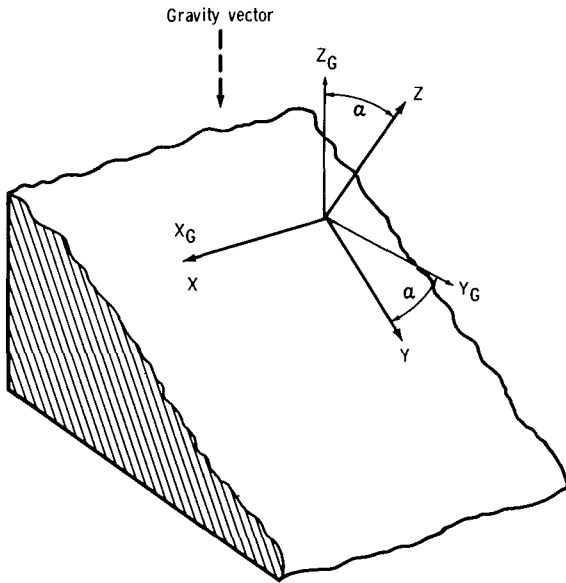
$$[T_{IG}] = \begin{bmatrix} 1 & 0 & 0 \\ 0 & \cos \alpha & \sin \alpha \\ 0 & -\sin \alpha & \cos \alpha \end{bmatrix} \quad (1)$$

Figure 1. - Gravity and inertial co-
ordinate system orientation.

Since equation (1) is an orthogonal transformation matrix, the transformation $\left[T_{GI}\right]$ from the gravity system to the inertial system is

$$\left[T_{GI}\right] = \left[T_{IG}\right]^{-1} = \left[T_{IG}\right]^{T} = \begin{bmatrix} 1 & 0 & 0 \\ 0 & \cos\alpha & -\sin\alpha \\ 0 & \sin\alpha & \cos\alpha \end{bmatrix} \tag{2}$$

Initial-touchdown-velocity input data are expressed in the gravity system and then transformed to the inertial system by the transformation $\left[T_{GI}\right]$.

Body Coordinate System (X_B-, Y_B-, and Z_B-Axes)

The body coordinate system is fixed in the landing vehicle so that the origin coincides with the idealized-rigid-vehicle center of mass, and the Z_B-axis is directed upward parallel to the vehicle vertical center line (fig. 2). The body system is related to the inertial system by the set of Euler angles θ_x, θ_y, and θ_z illustrated in figure 3.
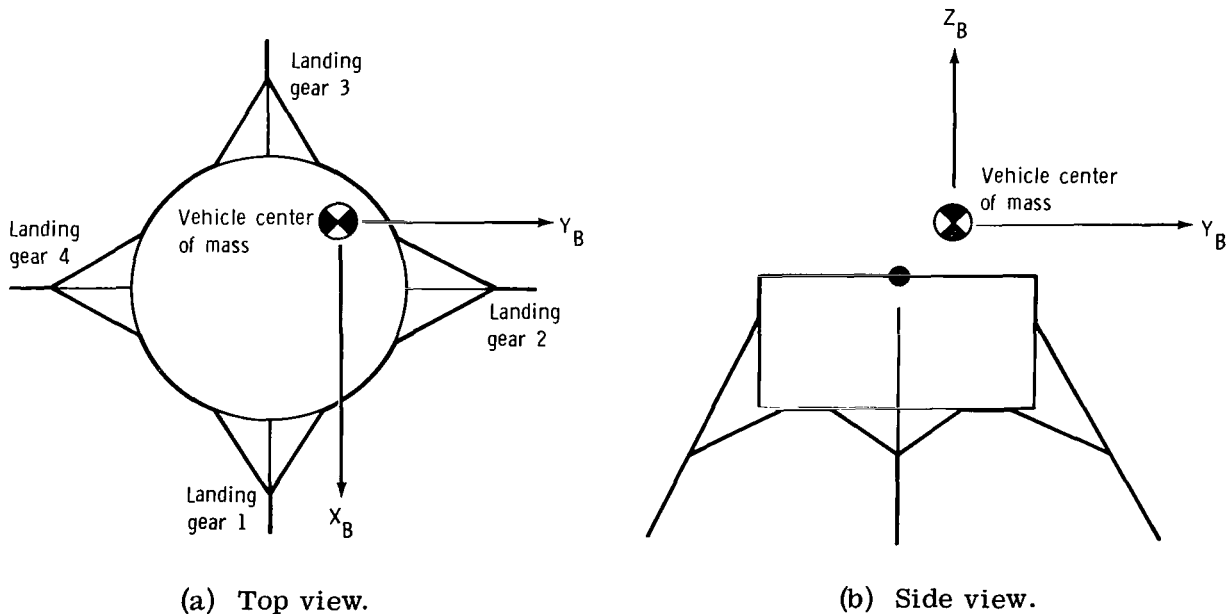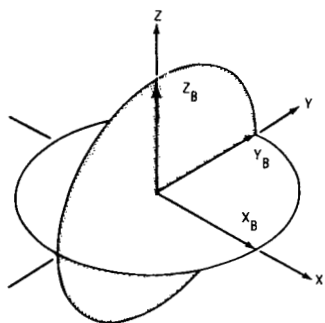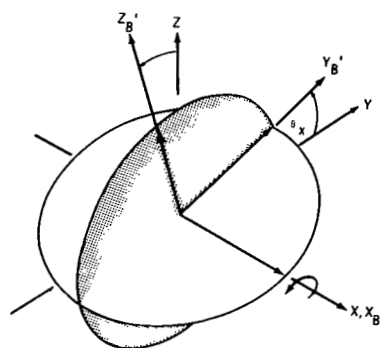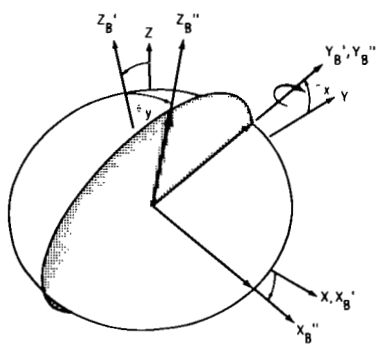

(a) Top view.   (b) Side view.

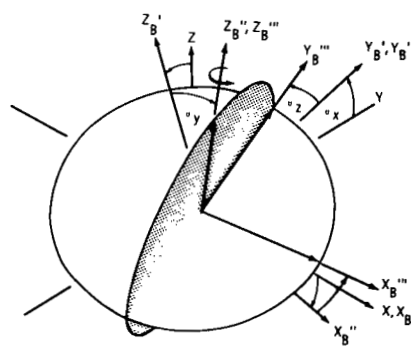Figure 2. - Orientation of the body coordinate system in the rigid vehicle.

(a) Body and inertial systems coinciding.

(b) Rotation about X_B-axis (θ_x).

(c) Rotation about Y_B'-axis (θ_y).

(d) Rotation about Z_B''-axis (θ_z).
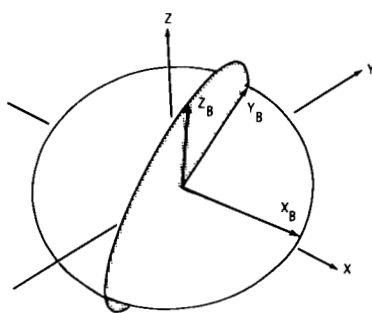
(e) Final orientation.

Figure 3. - Euler angle definition.

The rotation order is θ_x, θ_y, and θ_z, with each successive rotation taken about the indicated body axis in its position after the previous rotation. For example, the two coordinate systems can be oriented so that they coincide as shown in figure 3(a). The first rotation θ_x is about the X_B-axis as shown in figure 3(b). The next rotation θ_y is about Y_B', the new Y_B-axis position, as illustrated in figure 3(c). For the final rotation, the angle θ_z is rotated about Z_B'', the new Z_B-axis position, as indicated in figure 3(d). The final orientation of the body coordinate system with respect to the inertial coordinate system is shown in figure 3(e). These rotations can be considered to be a pitch-roll-yaw sequence for a pilot facing in the direction of the positive Y_B-axis.

The transformation $\begin{bmatrix} T_{BI} \end{bmatrix}$ which transforms vector components in the body system to vector components in the inertial system is

$$\begin{bmatrix} T_{BI} \end{bmatrix} = \begin{bmatrix} GOXX & -GOXY & GOXZ \\ GOYX & -GOYY & -GOYZ \\ -GOZX & GOZY & GOZZ \end{bmatrix} \tag{3}$$

where $GOXX = \cos \theta_y \cos \theta_z$

$GOXY = \cos \theta_y \sin \theta_z$

$GOXZ = \sin \theta_y$

$GOYX = \sin \theta_x \sin \theta_y \cos \theta_z + \cos \theta_x \sin \theta_z$

$GOYY = \sin \theta_x \sin \theta_y \sin \theta_z - \cos \theta_x \cos \theta_z$

$GOYZ = \sin \theta_x \cos \theta_y$

$GOZX = \cos \theta_x \sin \theta_y \cos \theta_z - \sin \theta_x \sin \theta_z$

$GOZY = \cos \theta_x \sin \theta_y \sin \theta_z + \sin \theta_x \cos \theta_z$

$GOZZ = \cos \theta_x \cos \theta_y$

This transformation is also orthogonal, and $\begin{bmatrix} T_{IB} \end{bmatrix}$ which transforms inertial system coordinates to body system coordinates is given by

$$\begin{bmatrix} T_{IB} \end{bmatrix} = \begin{bmatrix} T_{BI} \end{bmatrix}^T \tag{4}$$

19

Another important matrix transformation, which is employed, relates the rigid-vehicle angular rate vector components expressed in the body system to Euler angular rate components. The Euler angular rate components ($\dot{\theta}_x$, $\dot{\theta}_y$, and $\dot{\theta}_z$) are directed along the axis about which the respective Euler rotation (θ_x, θ_y, or θ_z) is made. This transformation is not orthogonal because the Euler angular rate components are not mutually orthogonal.

The transformation from body angular rates to Euler angular rates is given by

$$
\begin{bmatrix} T_{BE} \end{bmatrix} = \begin{bmatrix} \dfrac{\cos \theta_z}{\cos \theta_y} & -\dfrac{\sin \theta_z}{\cos \theta_y} & 0 \\[2em] \sin \theta_z & \cos \theta_z & 0 \\[2em] -\dfrac{\sin \theta_y \cos \theta_z}{\cos \theta_y} & \dfrac{\sin \theta_y \sin \theta_z}{\cos \theta_y} & 1 \end{bmatrix} \tag{5}
$$

The transformation from Euler angular rates to body angular rates is given by

$$
\begin{bmatrix} T_{EB} \end{bmatrix} = \begin{bmatrix} T_{BE} \end{bmatrix}^{-1} = \begin{bmatrix} \cos \theta_y \cos \theta_z & \sin \theta_z & 0 \\[1em] -\cos \theta_y \sin \theta_z & \cos \theta_z & 0 \\[1em] \sin \theta_y & 0 & 1 \end{bmatrix} \tag{6}
$$

Thus

$$
\begin{bmatrix} \dot{\theta}_x \\[1em] \dot{\theta}_y \\[1em] \dot{\theta}_z \end{bmatrix} = \begin{bmatrix} T_{BE} \end{bmatrix} \begin{bmatrix} \omega_x \\[1em] \omega_y \\[1em] \omega_z \end{bmatrix} \tag{7}
$$

where $\dot{\theta}_x, \dot{\theta}_y, \dot{\theta}_z$ = Euler angular rate components

$\omega_x, \omega_y, \omega_z$ = body angular rate components

20

A time derivative of equation (7) yields an expression for the time rate of change of Euler angular rate components.

$$
\begin{bmatrix} \ddot{\theta}_x \\ \ddot{\theta}_y \\ \ddot{\theta}_z \end{bmatrix} = \begin{bmatrix} T_{BE} \end{bmatrix} \begin{bmatrix} \dot{\omega}_x \\ \dot{\omega}_y \\ \dot{\omega}_z \end{bmatrix} + \left(\frac{d}{dt} \begin{bmatrix} T_{BE} \end{bmatrix} \right) \begin{bmatrix} \omega_x \\ \omega_y \\ \omega_z \end{bmatrix} \tag{8}
$$

For programing purposes, equation (8) can be reduced to the following more efficient form:

$$
\ddot{\theta}_x = \frac{\dot{\omega}_x \cos\theta_z - \dot{\omega}_y \sin\theta_z - 2\dot{\theta}_z \dot{\theta}_y + \dot{\theta}_y \omega_z}{\cos\theta_y} \tag{9a}
$$

$$
\ddot{\theta}_y = \dot{\omega}_x \sin\theta_z + \dot{\omega}_y \cos\theta_z + \dot{\theta}_x \dot{\theta}_z \cos\theta_y \tag{9b}
$$

$$
\ddot{\theta}_z = -\ddot{\theta}_x \sin\theta_y - \dot{\theta}_x \dot{\theta}_y \cos\theta_y + \dot{\omega}_z \tag{9c}
$$

Equations (9a) to (9c) express the angular acceleration components $\dot{\omega}_x$, $\dot{\omega}_y$, and $\dot{\omega}_z$ in a form that can be numerically integrated to yield the angular coordinates θ_x, θ_y, and θ_z (the three Euler angles), which are used to describe the orientation of the rigid vehicle in the inertial coordinate system.

A more common procedure for computing Euler angles is to integrate $\dot{\omega}_x$, $\dot{\omega}_y$, and $\dot{\omega}_z$ to obtain ω_x, ω_y, and ω_z and then to transform these angular rates by means of equation (7) to obtain equations for Euler angular rates (for example, as in reference 4). The Euler angular rates are then integrated to obtain Euler angles. However, this approach is not used in the mathematical procedure developed in this report. The formulation given by equations (9a) to (9c) is more convenient for the particular numerical integration procedure used to solve the equations of motion. This numerical integration procedure is discussed in a subsequent section of this report.

EQUATIONS OF MOTION

The landing vehicle is idealized as a rigid body of constant mass to which landing gear assemblies that have identical geometry and mass characteristics are attached. The mass of each landing gear assembly is assumed to be a point mass concentrated at the footpad of the assembly. Instead of using the actual mass of the landing gear assembly as the footpad mass, an "effective footpad mass" is computed so that the

effective footpad mass located at the footpad position approximates the inertia characteristics of the landing assembly. The effect of this approximation on the simulated landing dynamics has been studied in depth in reference 7. The conclusions in reference 7 imply that if the mass ratio of the vehicle landing gear assembly to the vehicle is small (approximately 1:50 for the LM), the effect of this approximation on the simulated landing performance is negligible.

The instantaneous position coordinates of the rigid-vehicle center of mass (X, Y, and Z) together with the instantaneous values of the Euler angles (θ_x, θ_y, and θ_z) specifying the orientation of the rigid vehicle, and the instantaneous position coordinates of the nth landing gear footpad XP_n, YP_n, and ZP_n in the inertial coordinate system allow for determination of the instantaneous geometry of the nth landing gear assembly. As will be explained in more detail in the following sections, a knowledge of instantaneous landing gear geometry allows the computation of the instantaneous forces acting on the rigid vehicle and on each of the landing gear footpads. Therefore, the equations of motion which must be solved in the simulation of the landing impact dynamics are the three translational equations of motion of the rigid-vehicle center of mass, the three rotational equations of motion of the idealized rigid vehicle, and the three translational equations of motion for each landing gear footpad.

The three translational equations of motion of the rigid-vehicle center of mass are obtained by the summation of all forces acting on the rigid vehicle and by the application of Newton's Laws of Motion.

$$\ddot{X} = \frac{FX}{M} + g_x \qquad (10)$$

$$\ddot{Y} = \frac{FY}{M} + g_y \qquad (11)$$

$$\ddot{Z} = \frac{FZ}{M} + g_z \qquad (12)$$

where FX, FY, FZ = summation of forces on the idealized rigid vehicle resolved along the X-, Y-, and Z-axes, respectively

M = mass of the idealized rigid vehicle

$\ddot{X}, \ddot{Y}, \ddot{Z}$ = inertial accelerations of rigid-vehicle center of mass

g_x, g_y, g_z = components of the gravitational acceleration vector expressed in the inertial coordinate system

The three rotational equations of motion express the time rate of change of the angular momentum vector of the rigid spacecraft in terms of Euler angles and Euler

angular rates. These equations of motion given as follows were developed in the previous section.

$$\ddot{\theta}_x = \frac{\dot{\omega}_x \cos \theta_z - \dot{\omega}_y \sin \theta_z - 2\dot{\theta}_z \dot{\theta}_y + \dot{\theta}_y \omega_z}{\cos \theta_y} \tag{9a}$$

$$\ddot{\theta}_y = \dot{\omega}_x \sin \theta_z + \dot{\omega}_y \cos \theta_z + \dot{\theta}_z \dot{\theta}_x \cos \theta_y \tag{9b}$$

$$\ddot{\theta}_z = -\ddot{\theta}_x \sin \theta_y - \dot{\theta}_x \dot{\theta}_y \cos \theta_y + \dot{\omega}_z \tag{9c}$$

where $\dot{\omega}_x$, $\dot{\omega}_y$, and $\dot{\omega}_z$ are the components of the angular acceleration vector expressed in the body coordinate system. These components are determined by solving the following Euler moment equations for rigid bodies (ref. 8).

$$T_x = I_{xx}\dot{\omega}_x - I_{xy}\dot{\omega}_y - I_{xz}\dot{\omega}_z + \left(-I_{xy}\omega_x - I_{yz}\omega_y + I_{zz}\omega_z\right)\omega_y$$
$$- \left(-I_{xy}\omega_x + I_{yy}\omega_y - I_{yz}\omega_z\right)\omega_z \tag{13}$$

$$T_y = -I_{xy}\dot{\omega}_x + I_{yy}\dot{\omega}_y - I_{yz}\dot{\omega}_z + \left(I_{xx}\omega_x - I_{xy}\omega_y - I_{yz}\omega_z\right)\omega_z$$
$$+ \left(I_{xz}\omega_x + I_{yz}\omega_z - I_{zz}\omega_z\right)\omega_y \tag{14}$$

$$T_z = -I_{xz}\dot{\omega}_x - I_{yz}\dot{\omega}_y + I_{zz}\dot{\omega}_z + \left(-I_{xy}\omega_x + I_{yy}\omega_y - I_{yz}\omega_z\right)\omega_x$$
$$+ \left(-I_{xx}\omega_x + I_{xy}\omega_y + I_{xz}\omega_z\right)\omega_y \tag{15}$$

where ω_x, ω_y, ω_z = angular rate vector components of the rigid vehicle expressed in the body coordinate system

I_{xx}, I_{yy}, I_{zz} = mass moments of inertia about the X_B-, Y_B-, and Z_B-axes, respectively

I_{xy} = cross product of inertia with respect to the X_B-Y_B plane

I_{xz} = cross product of inertia with respect to the X_B-Z_B plane

I_{yz} = cross product of inertia with respect to the Y_B-Z_B plane

T_x, T_y, T_z = sum of the torques about the X_B-, Y_B-, and Z_B-axes, respectively

The footpad equations of motion describe translational footpad motion only and are obtained by summing all forces acting on the effective footpad masses and by applying Newton's Laws of Motion. The equations have the general form given in the following three equations, although the actual equations solved may vary with the specific type of landing surface postulated. The actual equations used for various types of landing surfaces are explained in detail in later sections.

$$\ddot{XP}_n = \frac{1}{PMASS}\left(FXP_n - \frac{FGRND_n \dot{XP}_n}{\sqrt{\left(\dot{XP}_n\right)^2 + \left(\dot{YP}_n\right)^2}}\right) + g_x \tag{16}$$

$$\ddot{YP}_n = \frac{1}{PMASS}\left(FYP_n - \frac{FGRND_n \dot{YP}_n}{\sqrt{\left(\dot{XP}_n\right)^2 + \left(\dot{YP}_n\right)^2}}\right) + g_y \tag{17}$$

$$\ddot{ZP}_n = \frac{1}{PMASS}\left(FZP_n\right) + g_z \tag{18}$$

where XP_n, YP_n, ZP_n = instantaneous position coordinates of the nth footpad in the inertial coordinate system

PMASS = effective mass of each footpad

$FGRND_n$ = magnitude of a drag force on the nth footpad with direction opposite to the instantaneous sliding direction of the footpad in the X-Y plane

FXP_n, FYP_n, FZP_n = forces on the nth footpad in the X-, Y-, and Z-directions, respectively, which are independent of the instantaneous sliding direction of the footpad

g_x, g_y, g_z = components of the gravitational acceleration vector expressed in the inertial coordinate system

The equations of motion (eqs. (9a) to (12) and (16) to (18)) are solved by a numerical integration procedure. The initial conditions for these equations are specified in the following manner. The spacecraft attitude at the instant of impact is specified by the three Euler angles θ_x, θ_y, and θ_z. These angles determine which footpad is initially in contact with the landing surface, and this initial point of contact is taken to be the origin of the inertial coordinate system (0, 0, 0). The position of each footpad in the

body coordinate system prior to impact can be specified by known vehicle geometry. Let the vector expressed in body coordinates and directed from the origin of the body coordinate system to the footpad in contact with the surface be denoted by $\overrightarrow{BP}_n$. Then, the vector joining the origin of the inertial coordinate system and the origin of the body coordinate system is given by the vector transformation

$$\begin{bmatrix} X \\ Y \\ Z \end{bmatrix} = -\begin{bmatrix} T_{BI} \end{bmatrix} \overrightarrow{BP}_n \tag{19}$$

since the tip of $\overrightarrow{BP}_n$ is located at inertial system coordinates $(0, 0, 0)$. The three velocity components of the rigid-vehicle center of mass are specified in the gravity coordinate system and are then transformed into inertial system components by means of the transformation given in equation (2). Thus, the three initial inertial coordinates of the rigid-vehicle center of mass given by equation (19), together with the three velocity components at impact, comprise the initial conditions for the numerical integration of equations (10) to (12).

The angular rate vector components of the spacecraft at impact are initially specified in the body coordinate system and are then transformed to Euler angular rates by equation (7). These Euler rates, together with the initially specified Euler angles, provide initial conditions for the integration of equations (9a) to (9c). Equations (13) to (15) are solved as a set of simultaneous algebraic equations for the quantities $\dot{\omega}_x$, $\dot{\omega}_y$, and $\dot{\omega}_z$ at each integration step prior to the numerical integration of equations (9a) to (9c). After equations (9a) to (9c) are integrated, new values of ω_x, ω_y, and ω_z are computed by transforming the new Euler rates by means of the transformation given in equation (6).

The positions and velocities of the landing gear footpads are determined by integration of equations (16) to (18) only if the nth footpad is in contact with the surface. If the nth footpad is not in contact with the surface, the position and velocity of the footpad are computed by assuming the footpad to be rigidly connected to the vehicle. The initial conditions for equations (16) to (18) are taken to be the inertial position and velocity of each footpad at the instant the Z-coordinate of the respective footpad is computed to be less than or equal to zero. If a footpad breaks contact with the surface, the landing gear geometry is assumed to remain unchanged from the instant the footpad leaves the surface until it recontacts the surface, and during the period of no contact with the surface, the position and velocity of the footpad are computed as though the footpad were rigidly connected to the vehicle. At the instant of recontact with the surface, the footpad equations of motion are initialized as before.

NUMERICAL INTEGRATION OF THE EQUATIONS OF MOTION

It has been mentioned that the equations of motion are solved by a numerical integration procedure. There are many factors which should be considered in the selection of a particular method of numerical integration. Among these factors are the accuracy, speed, stability, integration-step-size control, and ease of adaptation of the method to the particular equations to be integrated. Among the more sophisticated methods now popular are (1) predictor-corrector methods that use backward difference formulas and that maintain a specified accuracy in the integration and (2) the well-known Runge-Kutta formulas. The predictor-corrector methods are cumbersome to use in problems where frequent changes in the integration step size are desirable. In attempting to maintain a specified accuracy, these methods will often perform an integration step forward, incur excessive integration error, and then waste the associated computations by making the same integration forward with a smaller step size. It was reasoned that because of the large number of computations involving the determination of landing gear geometry and forces necessary for each integration step, wasted integration steps could lead to unjustifiable amounts of computer time for landing simulations. Consequently, the predictor-corrector method was not used. To use a fourth-order Runge-Kutta formula for the integration of the rigid-vehicle equations of motion, it would be necessary to evaluate the landing gear geometry and associated force determination equations four times for each integration step. Since this large number of evaluations would also lead to very large amounts of computer time for the landing simulations, Runge-Kutta formulas were not used. A compromise integration scheme which was finally selected sacrifices a guaranteed numerical accuracy for a considerable gain in integration speed, while maintaining the desirable feature of variable step-size control.

The selection of the numerical integration method presented in the following paragraphs was influenced by several factors which are peculiar to the landing simulation. First, it was recognized that small integration steps would be necessary because of the abrupt on-off nature of some of the forces which occur during landing impact, such as those obtained from RCS jets, multiple landing gear impacts, and rocket engine nozzle impact with the landing surface. Second, if integration were performed with relatively large integration steps and if a footpad impacted the surface during an integration step, then the integration step would have to be discarded and attempted again with a smaller step size. Another characteristic of the forces experienced by the vehicle during landing is that except for the discrete occurrences of abrupt force level changes, there are intermediate periods where the force levels remain fairly constant.

These characteristics suggested that a simple method which assumed constant forces (or acceleration) over short integration steps could be expected to give reasonably accurate results. To accommodate those integration steps where abrupt force changes take place, it was assumed instead that the acceleration on the center of mass is a linear function of time during the integration step.

Taking equation (10) as an example, a linear variation of acceleration over time step Δt implies

$$\ddot{X}_{t_k + \Delta t} - \ddot{X}_{t_k} = \left(\frac{FX}{M}\right)_{t_k + \Delta t} - \left(\frac{FX}{M}\right)_{t_k} = c \, \Delta t \qquad (20)$$

where t_k is the time at the beginning of the kth integration step, and c is a constant for the integration step. If $\Delta t = t_{k+1} - t_k$, then the acceleration during the time step is described by

$$\ddot{X} = \ddot{X}_{t_k} + c\left(t - t_k\right) \qquad (21)$$

A first integration of equation (21) from t_k to $t_{k+1} = t_k + \Delta t$ yields

$$\dot{X}_{t_k + \Delta t} = \dot{X}_{t_k} + \ddot{X}_{t_k} \Delta t + \frac{1}{2} c(\Delta t)^2 \qquad (22)$$

A second integration of equation (21) yields

$$X_{t_k + \Delta t} = X_{t_k} + \dot{X}_{t_k} \Delta t + \frac{1}{2} \ddot{X}_{t_k} (\Delta t)^2 + \frac{1}{6} c(\Delta t)^3 \qquad (23)$$

An estimate of X and $\dot{X}$ at $t_k + \Delta t$ is obtained from equations (22) and (23) by assuming $c = 0$. With these estimates, new vehicle geometry, forces, and accelerations are computed, and the coefficient c is evaluated by computing FX/M at $t_k + \Delta t$ and then using equation (20) to obtain

$$c = \frac{(FX)_{t_k + \Delta t} - (FX)_{t_k}}{M \Delta t} \qquad (24)$$

Then, equations (22) and (23) are used to obtain corrected values for X and $\dot{X}$. A similar scheme is used for the integration of equations (9a) to (9c), (11), and (12). The footpad equations of motion are integrated by a standard fourth-order Runge-Kutta method where the magnitude of all forces on the footpads is assumed to be constant over an integration step, but where the variation in direction of the sliding velocity of the footpad during the integration step is taken into account.

The logic used to control integration step size for this particular touchdown dynamics problem is based on an "engineering decision," rather than on the usual truncation error checks used for determining step size for many variable step integration methods. This engineering decision is founded on the belief that as long as the amount of landing gear stroke or footpad movement is kept small (approximately 0.1 inch for an LM landing) during an integration step, the forces on the vehicle and the footpads

will not vary sufficiently so as to violate significantly the assumption of linear variation in acceleration over an integration time step. If the desired maximum allowable movement between footpads and the rigid-vehicle center of mass per integration step is specified by the input value DIST, then at any point in the integration, the integration step size for the next step Δt is computed from the relation

$$\Delta t = \frac{DIST}{VEL} \tag{25}$$

where VEL is the absolute value of the maximum relative velocity between the rigid-vehicle center of mass and the landing gear footpads. The value for Δt computed by equation (25) is used, unless this value exceeds a specified maximum integration step size or is less than a specified minimum step size.

IDEALIZATION OF LANDING GEAR GEOMETRY

It has been mentioned previously that once the instantaneous forces acting on the rigid vehicle are determined, solution of the equations of motion is possible. The most significant forces which act on the rigid spacecraft during touchdown are generated in the landing gear struts. Therefore, detailed representation of these strut forces is necessary to produce an accurate simulation of the vehicle landing dynamics. To represent landing gear strut forces accurately, a detailed simulation of landing gear articulation during impact is necessary.

The mathematical model of the soft-landing gear system considers two basic types of landing gear assemblies. One type is the cantilever gear presently used for the LM landing gear system (fig. 4(a)), and the other is the inverted tripod gear (fig. 4(b)). (The term "cantilever" in the name "cantilever gear" is incorrect in that the gear is not a cantilever in the geometric sense. The designers of this landing gear originally referred to it as the "bending gear" because of the bending of the primary strut under secondary strut loading. The name "bending gear" was not selected because it erroneously implied that strut bending was a primary function of the landing gear system.)

(a) Cantilever assembly. (b) Inverted tripod assembly.
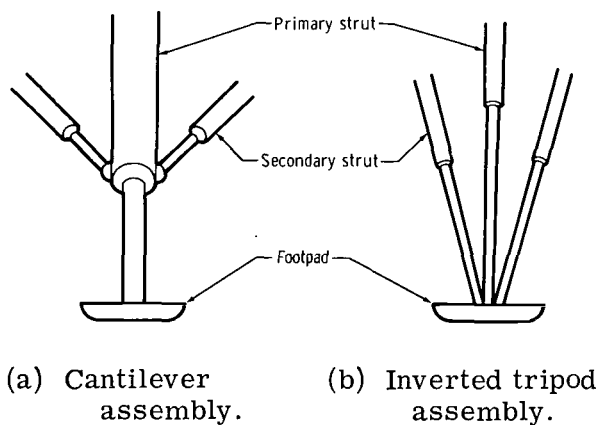
Figure 4. - Two types of landing gear assemblies.

The landing gear strut assembly in either of the two arrangements is composed of one primary strut and two secondary struts. Each secondary and primary strut is composed of an outer cylinder and an inner cylinder, with the inner cylinder telescoping into the outer cylinder. In the cantilever arrangement, the lower end of the secondary struts is attached to the lower end of the primary strut outer

cylinder. For the tripod assembly, the lower ends of the secondary struts are attached to the lower end of the primary strut inner cylinder. Since the mathematical simulation of the tripodal arrangement is a special case of the cantilever arrangement, the following analysis of the landing gear geometry is developed for the more general cantilever configuration. A typical cantilever assembly is depicted in figure 5 by a set of vectors.
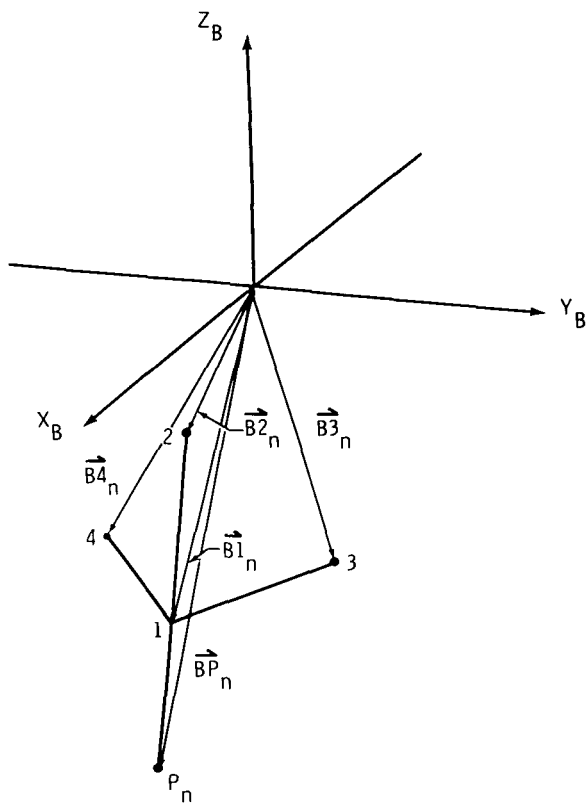
(a) Orientation of landing gear assembly in body coordinate system.
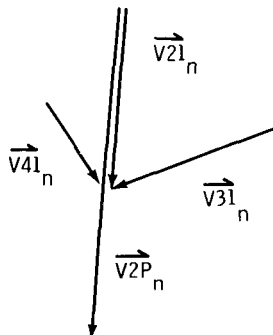
(b) Strut vectors.

Figure 5. – Landing gear strut vector diagram.

The landing gear represented in figure 5 is applicable to each of n landing gear assemblies; hence, n = 1, 2, 3, ... All numbered points in figure 5(a) are assumed to be ball-joint connections. Points 2, 3, and 4 are trunnion points where the primary strut and the secondary struts are joined to the idealized rigid structure. In the present discussion, these points are considered to be fixed points on the body. The point P_n, where the primary strut is joined to the footpad, can move in any direction as a result of stroking of primary and secondary struts. If the coordinates of P_n are known continually during a touchdown simulation, then vector equations can be constructed to define the instantaneous strut geometry, and subsequently, strut stroking velocities and strut lengths can be determined.

Every point in figure 5(a) can be represented by a position vector joining that point with the origin of the body coordinate system. Then the vector equivalents of points 4, 2, 3, 1, and P_n are $\vec{B4}_n$, $\vec{B2}_n$, $\vec{B3}_n$, $\vec{B1}_n$, and $\vec{BP}_n$, respectively, with body coordinates defined by

$$
\left.
\begin{aligned}
\vec{B4}_n &= \left[XB4_n, \; YB4_n, \; ZB4_n \right]^T \\[6pt]
\vec{B2}_n &= \left[XB2_n, \; YB2_n, \; ZB2_n \right]^T \\[6pt]
\vec{B3}_n &= \left[XB3_n, \; YB3_n, \; ZB3_n \right]^T \\[6pt]
\vec{B1}_n &= \left[XB1_n, \; YB1_n, \; ZB1_n \right]^T \\[6pt]
\vec{BP}_n &= \left[XBP_n, \; YBP_n, \; ZBP_n \right]^T
\end{aligned}
\right\} \qquad (26)
$$

For the present, assume that the components of BP_n are known. (The solution of the footpad equations of motion will yield the position vector $\overrightarrow{BP}_n$.) The vectors $\overrightarrow{B2}_n$, $\overrightarrow{B3}_n$, and $\overrightarrow{B4}_n$ are known from geometric definition of the vehicle. The vector between points 2 and P_n is $\overrightarrow{V2P}_n$, where

$$\overrightarrow{V2P}_n = \left[\left(XBP_n - XB2_n \right), \left(YBP_n - YB2_n \right), \left(ZBP_n - ZB2_n \right) \right]^T \tag{27}$$

The modulus of the vector $\overrightarrow{V2P}_n$, denoted by $V2P_n$, determines the instantaneous length of the primary strut. The vector $\overrightarrow{V2P}_n$ unitized is given by

$$\widehat{V2P}_n = \frac{\overrightarrow{V2P}_n}{V2P_n} \tag{28}$$

The vector $\overrightarrow{B1}_n$ is determined from the vector equation

$$\overrightarrow{B1}_n = \overrightarrow{V21}_n + \overrightarrow{B2}_n \tag{29}$$

where

$$\overrightarrow{V21}_n = \widehat{V2P}_n \left(L21_n \right) \tag{30}$$

and the distance $L21_n$ between points 2 and 1 is constant. In the tripodal arrangement, point 1 coincides with point P_n; therefore, $\overrightarrow{B1}_n$ is equal to $\overrightarrow{BP}_n$, and equations (29) and (30) are not necessary. (Of course, in the tripodal arrangement, $L21_n$ is not constant.) The vectors joining points 3 and 4 to point 1 are computed from

$$\left. \begin{aligned} \overrightarrow{V31}_n &= \overrightarrow{B1}_n - \overrightarrow{B3}_n \\ \overrightarrow{V41}_n &= \overrightarrow{B1}_n - \overrightarrow{B4}_n \end{aligned} \right\} \tag{31}$$

30

The lengths of vectors $\overrightarrow{V31}_n$ and $\overrightarrow{V41}_n$ yield the instantaneous secondary strut lengths. The following equations define the unit vectors of equations (31).

$$\left.\begin{aligned}
\widehat{V31}_n &= \frac{\overrightarrow{V31}_n}{\overline{V31}_n} \\[2em]
\widehat{V41}_n &= \frac{\overrightarrow{V41}_n}{\overline{V41}_n}
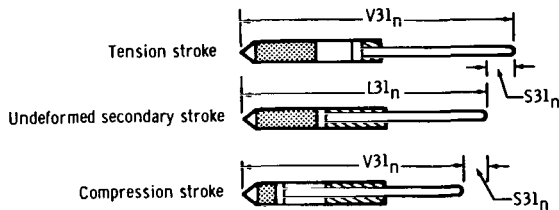\end{aligned}\right\} \tag{32}$$

The amount of stroke in each strut of the landing gear is required for determining axial forces in the struts. Figure 6 shows the primary and secondary struts in stroked and unstroked positions. If the undeformed lengths of the primary and secondary struts are denoted by $L2P_n$ and by $L31_n$ and $L41_n$, respectively, the instantaneous strokes of each are given by
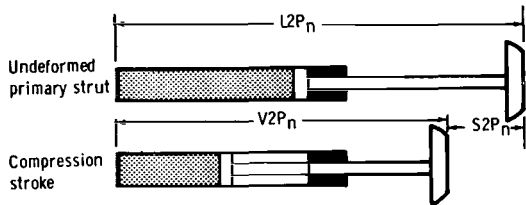
$$S2P_n = V2P_n - L2P_n \tag{33}$$

and

$$\left.\begin{aligned}
S31_n &= V31_n - L31_n \\[1em]
S41_n &= V41_n - L41_n
\end{aligned}\right\} \tag{34}$$

The compression stroke of a secondary strut is a negative quantity, and a tension stroke is a positive quantity.

(a) Primary strut.

(b) Secondary strut.

Figure 6. - Stroked and unstroked primary and secondary struts.

FORCES IN THE LANDING GEAR STRUTS

The problem of accounting for axial forces in the landing gear struts is rather involved because of force contributions from various sources. The various sources contributing to the landing gear strut forces are analyzed separately, summed, and resolved at the landing gear footpad.

Crushable-Type Shock Absorbers

The primary type of shock-attenuation mechanism for the LM landing gear system is a sequence of crushable metal honeycomb cartridges housed inside the landing gear struts. These cartridges collapse at a constant load when the landing gear struts are stroked. Several honeycomb strengths may be stacked in series to form a desired load-stroke output. The present analysis provides for a maximum of three cartridges in the primary struts and four cartridges in each secondary strut. The primary strut has shock-attenuation capability in compression stroking only, and the secondary struts have shock-attenuation capability in both tension and compression stroking. Figure 7 illustrates a typical honeycomb configuration for a primary and secondary strut assembly.
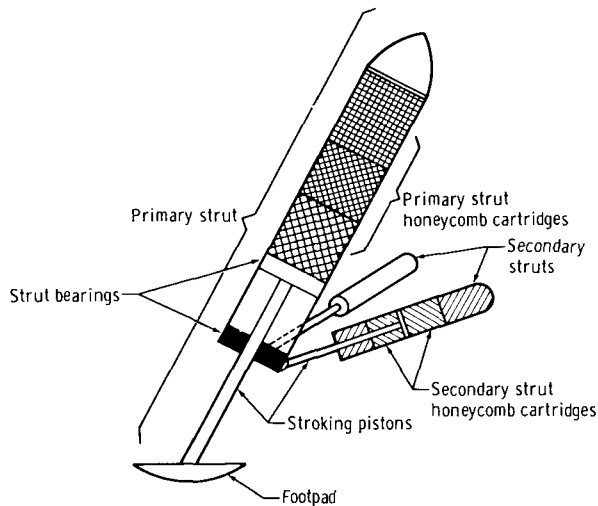
Honeycomb material can be designed to fail at a constant load as the honeycomb material is crushed. If this constant load is predetermined, characteristic relationships between strut axial loads and strut strokes can be described by a load-stroke diagram. A typical load-stroke diagram for the primary strut is shown in figure 8.

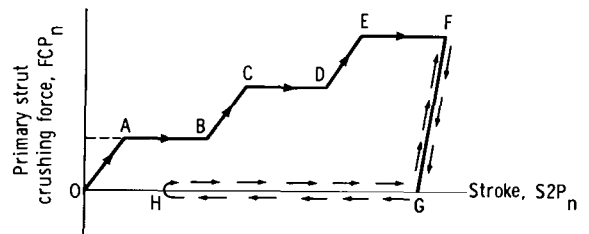Figure 7. - Primary and secondary strut crushable shock absorbers.

Figure 8. - Primary strut load-stroke diagram.

The primary struts have only compression-type crushing of the honeycomb cartridges. Tension loads are due to friction. The honeycomb cartridge loads are modeled in the following manner. In figure 8, the unstroked primary strut begins at station 0 and undergoes compression stroking. The strut load will increase linearly with stroke to the station A. The plateau denoted between stations A and B represents the failure load of the weakest or first-stage honeycomb cartridge. When the primary strut is stroked to station B, the first stage of the honeycomb cartridge has been exhausted. As the primary strut is stroked past station B, the load will again build up linearly with stroke until the second plateau is reached at station C. The plateaus between stations C and D and between stations E and F represent failure loads of the second- and third-stage honeycomb cartridges. If the primary strut begins to extend after undergoing compression stroking, the honeycomb load in the strut will reduce linearly. This reduction in load is shown in figure 8 along the path from station F to station G. If the primary strut continues to extend, the honeycomb load will go to zero at station G and will remain at zero if further elongation occurs. If the primary strut

starts to compress again, the strut will compress under zero load until station G is reached, whereupon the load will increase linearly from station G to station F. The unloading of the honeycomb from station F to station G is associated with elastic rebound of the honeycomb cartridge and may occur at any point in the load-stroke diagram.

The secondary struts are designed such that compression and tension honeycomb forces can be generated. A typical secondary strut load-stroke diagram is shown in figure 9. The secondary strut load-stroke characteristics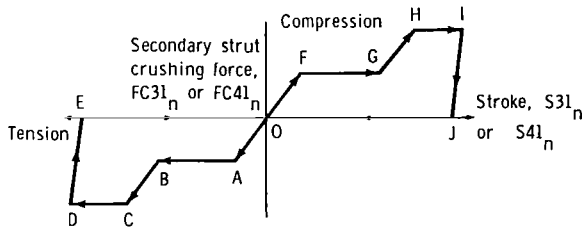 are similar to those of the primary strut. The undeformed secondary strut starts with zero honeycomb load at station zero and strokes in tension or compression with a linear buildup in load to station A or F. The plateaus defined by stations A and B, stations C and D, stations F and G, and stations H and I represent the failure load of the particular honeycomb cartridge. The elastic rebound is denoted by the paths from stations D to E and from stations I to J. A zero load between stations E and J is produced after the honeycomb material between stations E and J has been crushed.

Figure 9. - Secondary strut load-stroke diagram.

Modification of the Strut Load-Stroke Diagrams Because of Structural Elasticity

The position of the primary and the secondary strut attachment points (or trunnion points) on the spacecraft structure are assumed to be fixed in the body coordinate system. In reality, landing gear strut loads are transmitted through these attachment points, deforming the spacecraft structure and subsequently causing changes in the position of the attachment points in the body coordinate system. This deformation is important in that it effectively softens the elastic character of the honeycomb shock absorbers and has the capability to store energy. The influence of the structural deformation on the spacecraft touchdown dynamics can be approximated by idealizing the strut-structure system to be as shown in figure 10. This idealization allows for the modification of the honeycomb cartridge load-stroke diagram to account for the structural deformation.
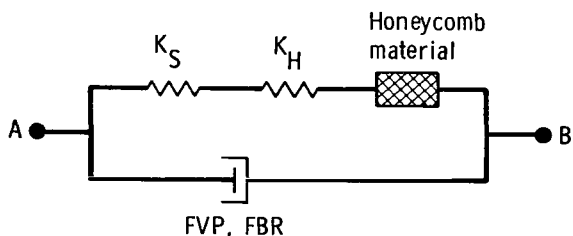
In figure 10, the spring constant K_S is representative of the slope of the load-deflection curve of the spacecraft structure at the trunnion point and is assumed to be constant. The spring constant K_H is representative of the elastic property of the honeycomb shock-absorber material.

Figure 10. - Idealized landing gear strut.

The terms FVP and FBR are the viscous and friction forces, respectively, present during strut stroking. Points A and B in figure 10 are analogous to the end points of the struts.

For the secondary struts, the structural spring constant K_S is made up of two factors, the spacecraft structural elasticity and the primary strut bending elasticity. The primary strut bending characteristics are functions of strut length and strut loads, which vary during a landing. The primary strut bending and its influence on strut load-stroke properties are discussed later in this section.

The honeycomb cartridge load-stroke diagram is first modified to account for the spacecraft structural deformation by computing an equivalent spring rate for springs (K_S and K_H) in series. The following equation is used to compute the modified onset honeycomb spring rates.

$$\left.\begin{aligned}
K'_{P,o} &= \frac{K_{TP}K_{P,o}}{K_{TP} + K_{P,o}} \\[2mm]
K'_{ST,o} &= \frac{K_{TS}K_{ST,o}}{K_{TS} + K_{ST,o}} \\[2mm]
K'_{SC,o} &= \frac{K_{TS}K_{SC,o}}{K_{TS} + K_{SC,o}}
\end{aligned}\right\} \tag{35}$$

where $K'_{P,o}$ = modified onset compression spring rate for the primary struts

$K'_{ST,o}$ = modified onset tension spring rate for the secondary struts

$K'_{SC,o}$ = modified onset compression spring rate for the secondary struts

K_{TP} = trunnion-point spring rate at the primary strut-structure attachment point

K_{TS} = trunnion-point spring rate at the secondary strut-structure attachment point

$K_{P,o}$ = primary strut onset spring rate without trunnion-point elasticity

$K_{ST,o}$ = secondary strut onset spring rate in tension stroking without trunnion-point elasticity

$K_{SC,o}$ = secondary strut onset spring rate in compression stroking without trunnion-point elasticity

Similarly, the modified primary and secondary strut backoff spring rates are given by the following equations.

$$
\left.
\begin{aligned}
K'_{P,B} &= \frac{K_{TP}K_{P,B}}{K_{TP} + K_{P,B}} \\[2ex]
K'_{ST,B} &= \frac{K_{TS}K_{ST,B}}{K_{TS} + K_{ST,B}} \\[2ex]
K'_{SC,B} &= \frac{K_{TS}K_{SC,B}}{K_{TS} + K_{SC,B}}
\end{aligned}
\right\}
\tag{36}
$$

where $K'_{P,B}$ = modified backoff compression spring rate for the primary struts

$K'_{ST,B}$ = modified backoff tension spring rate for the secondary struts

$K'_{SC,B}$ = modified backoff compression spring rate for the secondary struts

$K_{P,B}$ = primary strut backoff spring rate without trunnion-point elasticity

$K_{ST,B}$ = secondary strut backoff spring rate in tension stroking without trunnion-point elasticity

$K_{SC,B}$ = secondary strut backoff spring rate in compression stroking without trunnion-point elasticity

The primary and secondary strut load-stroke diagrams which have been modified to include the structural deformation are shown in figure 11.

The delta displacements shown on figure 11 represent the deformation of the spacecraft structure at the trunnion points caused by loading of the primary and secondary struts. The delta displacement of the modified primary strut load-stroke diagram is calculated by the equation

$$
\delta_P = \frac{FP1}{K_{TP}}
\tag{37}
$$

where FP1 is the first-stage crushing force of the honeycomb cartridge in the primary struts. Similarly, the delta displacements for the tension side of the modified secondary strut load-stroke diagram are calculated by

$$
\delta_T = \frac{FST1}{K_{TS}}
\tag{38}
$$

35
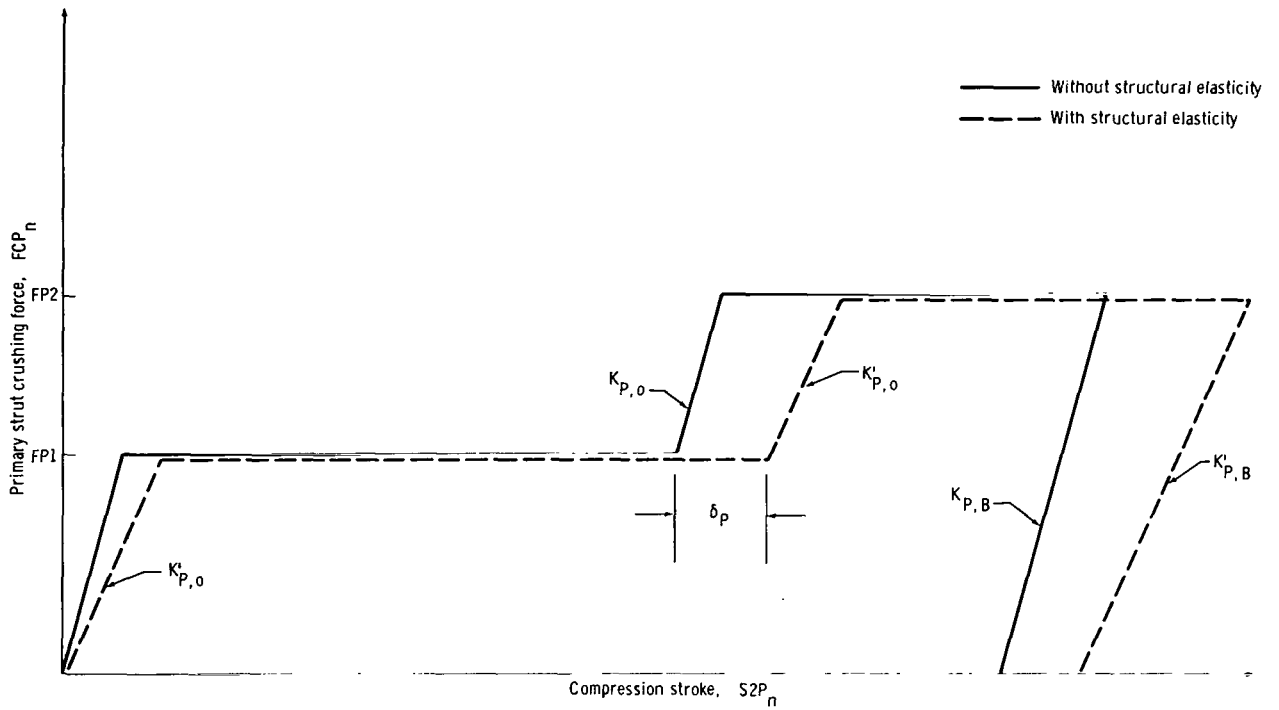
(a) Modified primary strut load-stroke diagram.
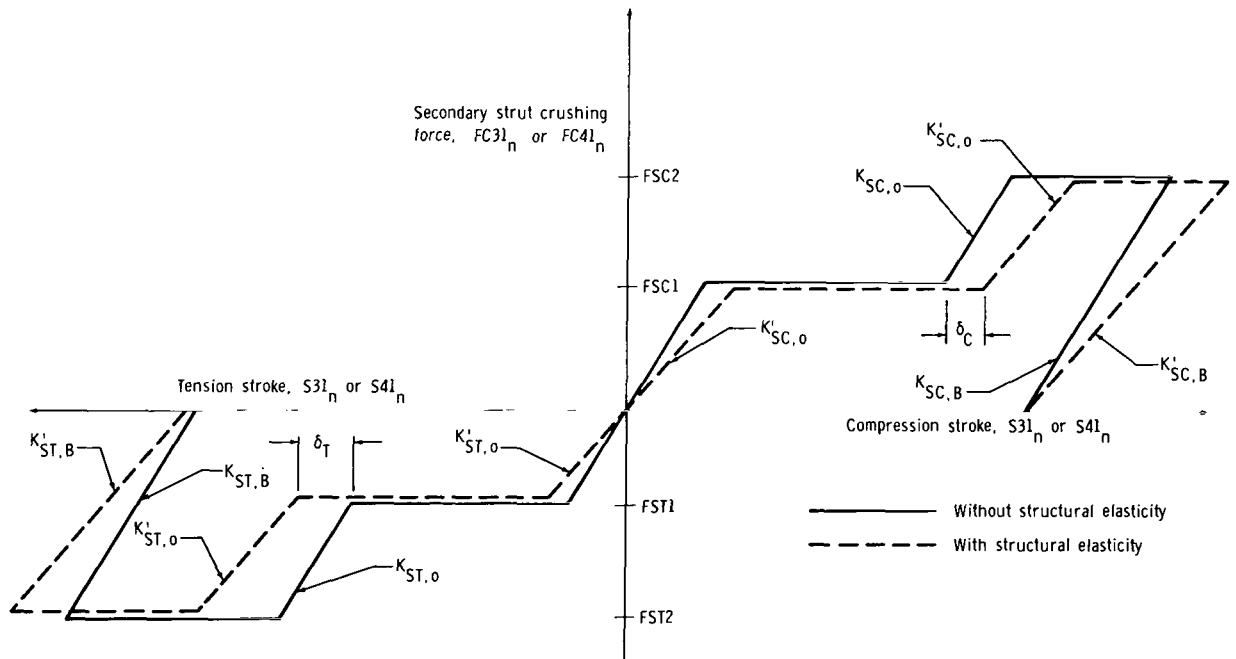
(b) Modified secondary strut load-stroke diagram.

Figure 11. - Structural elasticity modification for strut load-stroke diagram.

36

and for the compression side are calculated by

$$\delta_C = \frac{FSC1}{K_{TS}}$$ (39)

where FST1 and FSC1 are the first-stage crushing forces of the honeycomb cartridges for tension and compression stroking, respectively, of the secondary struts. The modified strut load-stroke diagrams as shown in figure 11 are used as input data to the computer.

A second modification in the secondary strut load-stroke diagram is made to account for the bending influence of the primary strut. This modification is made internally and continuously during the computer simulation. The position of the attachment point of the secondary struts on the primary strut is assumed to be fixed on the idealized rigid primary strut axis. However, because of the primary and secondary strut loads on the primary strut, the primary strut will undergo bending. The bending of the primary strut will cause the secondary strut attachment point to be deflected off the idealized rigid primary strut axis. If the assumption is made that the attachment point deforms elastically and linearly under load and according to the idealization as shown in figure 10, the primary strut bending influence on spacecraft touchdown dynamics can be approximated by a modification of the secondary strut load-stroke diagram.

The primary strut is treated as a uniform beam whose elastic axis is defined by simple beam theory. The governing differential equation that defines the shape of the beam is

$$EI \frac{d^2\eta}{ds^2} = M(s)$$ (40)

where
s = position coordinate along the length of the primary strut

η = deflection of the center line of the beam

EI = constant bending stiffness

M(s) = bending moment

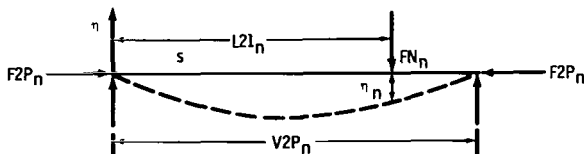The forces on the primary strut are idealized as shown in figure 12.

Figure 12. - Primary strut bending mode.

The force $F2P_n$ is an axial force produced by the compression stroking of the primary strut. The force FN_n is the normal component of the secondary strut honeycomb forces acting on the primary strut at the secondary-to-primary strut attachment point. This attachment point

corresponds to $s = L21_n$. By writing the bending moment $M(s)$ as a function of $F2P_n$, FN_n, and s, equation (40) is expanded to

$$EI \frac{d^2\eta}{ds^2} + \left(F2P_n\right)\eta = \left(FN_n\right)\left(1 - \frac{L21_n}{V2P_n}\right)s \quad \text{for} \quad 0 < s < L21_n \tag{41}$$

and

$$EI \frac{d^2\eta}{ds^2} + \left(F2P_n\right)\eta = \left(FN_n\right)\left(L21_n\right)\left(1 - \frac{s}{V2P_n}\right) \quad \text{for} \quad L21_n < s < V2P_n \tag{42}$$

Solving equations (41) and (42) for the deflection η and evaluating η at $s = L21_n$ yields

$$\eta_n = \frac{FN_n \sin^2\left(L21_n\sqrt{\frac{F2P_n}{EI}}\right)}{\left[F2P_n\sqrt{\frac{F2P_n}{EI}} \sin\left(L21_n\sqrt{\frac{F2P_n}{EI}}\right)\right]} - \frac{FN_n\left(L21_n\right)^2}{F2P_n\left(V2P_n\right)} \tag{43}$$

As the axial force $F2P_n$ approaches zero, the first and second terms of equation (43) approach plus and minus infinity, respectively. This situation introduces numerical error in the calculation of η when using equation (43). Therefore, when the primary strut compression force $F2P_n$ becomes arbitrarily small, it is assumed to be zero and equations (41) and (42) reduce to

$$EI \frac{d^2\eta}{ds^2} = FN_n\left(1 - \frac{L21_n}{V2P_n}\right)s \quad \text{for} \quad 0 < s < L21_n \tag{44}$$

and

$$EI \frac{d^2\eta}{ds^2} = FN_n\left(L21_n\right)\left(1 - \frac{s}{V2P_n}\right) \quad \text{for} \quad L21_n < s < V2P_n \tag{45}$$

38

Solving equations (44) and (45) for the deflection η at $s = L21_n$ yields

$$\eta_n = -\frac{FN_n}{6\left(V2P_n\right)EI}\left[\left(V2P_n - L21_n\right)\left(L21_n\right)\right]^2 \qquad (46)$$

Hence, if the primary strut compression force is large, equation (43) is used to compute the primary strut deflection at $s = L21_n$, and if the primary strut compression force is small, equation (46) is used to compute the primary strut deflection.

The deflection of the primary strut caused by axial and normal forces is assumed to be in the direction of the normal force. When a static bending deflection is produced in the primary strut at its secondary strut attachment point, an apparent change in the length of each idealized secondary strut is produced. This change in length $\delta_{i,n}$ of the ith secondary strut in the nth landing gear assembly is computed by

$$\left.\begin{aligned}\delta_{3,n} &= \eta_n\left(\widehat{FN}_n \cdot \widehat{V31}_n\right)\\\delta_{4,n} &= \eta_n\left(\widehat{FN}_n \cdot \widehat{V41}_n\right)\end{aligned}\right\} \qquad (47)$$

where $\quad\eta_n$ = primary strut deflection at point $s = L21_n$ on the nth primary strut (computed from eqs. (43) or (46))

$\widehat{FN}_n$ = unit vector directed along the normal force $\overrightarrow{FN}_n$

$\widehat{V31}_n, \widehat{V41}_n$ = unit vectors directed along the secondary struts

$\delta_{i,n}$ = apparent change in length of ith secondary strut as a result of nth primary strut bending

The deflection of the primary strut as a result of bending caused by secondary strut forces is assumed to be a linear function of the secondary strut honeycomb force. This assumption along with the idealization presented in figure 10 allows for the calculation of an equivalent spring rate for the secondary-to-primary-strut attachment points

to account for primary strut bending. The spring rates $KB3_n$ and $KB4_n$ for each secondary strut $V31_n$ and $V41_n$, which account for primary strut bending, are calculated by the following equations.

$$\left. \begin{aligned} KB3_n &= \frac{FC31_n}{\delta_{3n}} \\[1em] KB4_n &= \frac{FC41_n}{\delta_{4n}} \end{aligned} \right\} \tag{48}$$

where $FC31_n$ and $FC41_n$ are secondary strut honeycomb forces.

The secondary strut bending spring rates $KB3_n$ and $KB4_n$ change during the landing because of landing gear strut articulation and because of varying primary and secondary strut shock-absorber loads. For this reason, the bending spring rates and the secondary strut load-stroke diagrams are continually updated throughout a landing simulation by computing η_n from either equation (43) or equation (46) and then evaluating equations (47) and (48).

Viscous Forces

The mathematical model of the landing gear strut force attenuation mechanism has velocity-dependent forces. These forces act in a direction opposite to the strut stroking velocity and are added algebraically to other axial forces occurring in the struts. This arrangement gives considerable flexibility in modeling a landing gear strut shock-absorption characteristic. The landing gear strut velocity-dependent forces are described by the equations

$$\left. \begin{aligned} FVP_n &= CP\left(\dot{V2P}_n\right)^{\gamma_p} \\[1em] FV31_n &= CS\left(\dot{V31}_n\right)^{\gamma_s} \\[1em] FV41_n &= CS\left(\dot{V41}_n\right)^{\gamma_s} \end{aligned} \right\} \tag{49}$$

where $\quad FVP_n =$ stroking-velocity-dependent force in the nth landing gear primary strut

$$\text{FV31}_n, \text{FV41}_n = \text{stroking-velocity-dependent forces in the } n^{\text{th}} \text{ landing gear secondary struts}$$

$$\dot{\text{V2P}}_n, \dot{\text{V31}}_n, \dot{\text{V41}}_n = \text{stroking velocities of the primary and secondary struts}$$

$$\text{CP, CS} = \text{coefficients of the strut stroking velocities used to model a given force-velocity characteristic}$$

$$\gamma_p, \gamma_s = \text{exponents of the strut stroking velocities used to model a given force-velocity characteristic}$$

Each landing gear strut is allowed to have individual velocity-dependent force characteristics defined by data input for the various parameters in equation (49).

RESOLUTION OF FORCES AT THE FOOTPADS

Unit vectors which yield the instantaneous direction of each strut in the body coordinate system have previously been given by equations (28) and (32). If these unit vectors are multiplied by the scalar magnitudes of the axial forces determined for each strut, the force vectors applied to the footpads by the landing gear can be determined.

Let $\overrightarrow{\text{F2P}}_n$ be the instantaneous axial force in the primary strut inner cylinder of the nth gear assembly. Its magnitude is composed of

$$\text{F2P}_n = \text{FCP}_n + \text{FVP}_n + \text{FBR}_n \tag{50}$$

where FCP_n = force determined from primary strut shock-absorber load-stroke characteristics

FVP_n = primary strut viscous or stoking-velocity-dependent force

FBR_n = primary strut bearing friction force (developed in the following section)

Let the instantaneous axial forces in the inner cylinder of the secondary struts be denoted by $\overrightarrow{\text{F31}}_n$ and $\overrightarrow{\text{F41}}_n$. The directions of these forces are colinear with the previously defined vectors $\overrightarrow{\text{V31}}_n$ and $\overrightarrow{\text{V41}}_n$ shown in figure 5(b), and their magnitudes are given by

$$\left.\begin{array}{l} \text{F31}_n = \text{FC31}_n + \text{FV31}_n \\[1em] \text{F41}_n = \text{FC41}_n + \text{FV41}_n \end{array}\right\} \tag{51}$$

where $FC31_n$, $FC41_n$ = forces from secondary strut load-stroke characteristics

$FV31_n$, $FV41_n$ = secondary strut viscous or stroking-velocity-dependent forces

These forces are applied to the lower end of the primary strut outer cylinder. Figure 13(a) shows the axial strut forces. The primary strut bearing friction forces are determined from the normal loads on the primary strut bearing surfaces. The method for computing bearing loads is developed later in this section.

Let

$$\overrightarrow{FS}_n = \overrightarrow{F31}_n + \overrightarrow{F41}_n \tag{52}$$

be the vector sum of the secondary strut forces acting on the primary strut (fig. 13). The inertia properties of the landing gear assembly are represented by a mass concentrated at the ball joint of the landing gear footpad. This concentrated mass is referred to as the effective footpad mass. The magnitude of the effective footpad mass is determined to approximate the inertia characteristics of the landing gear assembly. The assumptions involved in this idealization of the mass properties of the landing gear assembly are discussed in reference 7.

(a) Axial strut forces.

(b) Forces and moments on the primary strut caused by secondary strut forces.
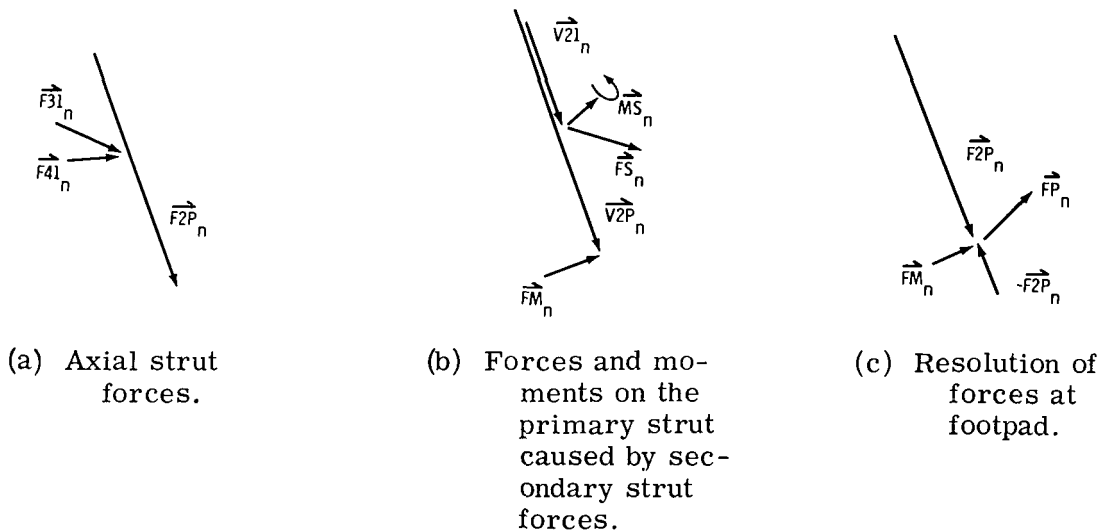
(c) Resolution of forces at footpad.

Figure 13. - Forces applied to the footpad.

The idealization considers the gear struts to be massless so that moments on the primary strut are computed without regard to rotational accelerations. Thus

$$\overrightarrow{V2P}_n \times \overrightarrow{FM}_n = -\overrightarrow{V21}_n \times \overrightarrow{FS}_n \tag{53}$$

Let

$$\overrightarrow{V21}_n \times \overrightarrow{FS}_n = \overrightarrow{MS}_n \tag{54}$$

where $\overrightarrow{MS}_n$ is a moment vector perpendicular to the primary strut and to $\overrightarrow{FS}_n$ as shown in figure 13(b). Since $\overrightarrow{FM}_n$ is normal to the primary strut at the footpad, the modulus of the left-hand side of equation (53) is

$$\left| \overrightarrow{V2P}_n \times \overrightarrow{FM}_n \right| = \left(V2P_n \right)\left(FM_n \right) \sin \frac{\pi}{2} = \left(V2P_n \right)\left(FM_n \right) \tag{55}$$

and FM_n is given by

$$FM_n = \frac{MS_n}{V2P_n} \tag{56}$$

The components of $\overrightarrow{FM}_n$ in the body coordinate system can be obtained by constructing a unit vector normal to both the primary strut and the moment vector $\overrightarrow{MS}_n$. Thus

$$\widehat{FM}_n = \frac{\overrightarrow{V2P}_n \times \overrightarrow{MS}_n}{\left(V2P_n \right)\left(MS_n \right)} \tag{57}$$

and

$$\overrightarrow{FM}_n = \left(\widehat{FM}_n \right) FM_n \tag{58}$$

Bearing Friction Analysis

The outer cylinder of the primary strut houses the stroking piston and bearings as shown in figure 14. The forces $\overrightarrow{F1}_n$ and $\overrightarrow{F2}_n$ are the normal forces generated at the bearings, and their magnitudes depend on the magnitude of FM_n. Since $\overrightarrow{F1}_n$, $\overrightarrow{F2}_n$, and $\overrightarrow{FM}_n$ are coplanar, scalar moment equations for static equilibrium of the inner
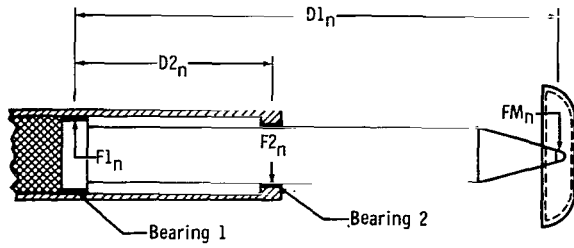
Figure 14. - Primary strut internal bearings.

cylinder may be written. Summing moments about bearing 1 yields

$$FM_n\left(D1_n\right) - F2_n\left(D2_n\right) = 0 \tag{59}$$

where $D1_n$ and $D2_n$ are the distances defined in figure 14. The length of the inner cylinder $D1_n$ is a constant, and $D2_n$ is determined from an initial bearing separation and from the compression stroke $S2P_n$ of the primary strut. The magnitude of the bearing force $F2_n$ is computed from

$$F2_n = \frac{FM_n\left(D1_n\right)}{D2} \tag{60}$$

Summing moments about bearing 2 yields

$$FM_n\left(D1_n - D2_n\right) - F1_n\left(D2_n\right) = 0 \tag{61}$$

and

$$F1_n = \frac{FM_n\left(D1_n - D2_n\right)}{D2_n} \tag{62}$$

The magnitude of the bearing friction force FBR_n can now be calculated from

$$FBR_n = \mu_B\left(F1_n + F2_n\right) \tag{63}$$

where μ_B is the bearing friction coefficient for both bearings. The direction of the bearing friction force is taken to be opposite to the stroking direction of the strut.

Total Forces and Moments From Landing Gear

With the bearing friction force now determined, all the terms on the right-hand side of equation (53) are known, and subsequently, $\overrightarrow{F2P}_n$ can be obtained from

$$\overrightarrow{F2P}_n = \widehat{V2P}_n\left(F2P_n\right) \tag{64}$$

where the unit vector $\widehat{V2P}_n$ is given by equation (28). The total instantaneous force transmitted to the footpads by primary and secondary struts (fig. 13(c)) can therefore be represented by

$$\overrightarrow{FP}_n = \overrightarrow{F2P}_n + \overrightarrow{FM}_n \tag{65}$$

The resultant torque $\overrightarrow{TCMG}$ on the rigid-vehicle center of mass due to landing gear strut loads is calculated by the following equation. (For the LM landing system, m = 4.)

$$\overrightarrow{TCMG} = \sum_{n=1}^{m}\left(\overrightarrow{BP}_n \times -\overrightarrow{FP}_n\right) \tag{66}$$

where $\overrightarrow{BP}_n$ is the vector from the rigid-vehicle center of mass to the footpad of the nth gear assembly, and $-\overrightarrow{FP}_n$ is the reaction force applied to the vehicle as a result of $\overrightarrow{FP}_n$. The vector $\overrightarrow{TCMG}$ is expressed in the body coordinate system.

The translational equations of motion for the rigid-vehicle center of mass are written with respect to the inertial coordinate system; therefore, it is necessary to express the resultant force $-\overrightarrow{FP}_n$ in the inertial system to obtain the inertial acceleration of the rigid-vehicle center of mass. By using the transformation given by equation (3), $-\overrightarrow{FP}_n$ expressed in the inertial system is

$$\overrightarrow{FPI}_n = -\left[T_{BI}\right]\overrightarrow{FP}_n \tag{67}$$

The sum of the landing gear forces acting on the rigid-vehicle center of mass expressed in the inertial coordinate system is then

$$\overrightarrow{FCMG} = \sum_{n=1}^{m} \overrightarrow{FPI}_n \tag{68}$$

The forces and torques applied to the rigid-vehicle center of mass by the landing gear have now been developed. Landing gear forces applied to the footpads have also been determined and will be used in the discussion of footpad motion on various landing surfaces in a later section.

ENGINE THRUST AND NOZZLE-CRUSHING FORCES

Certain spacecraft landing procedures may result in the descent-stage rocket engine thrust forces being present during the touchdown. Since these forces can be significant, their influence on spacecraft landing performance must be considered. The engine thrust forces are usually in a shutdown transient phase at some point in the touchdown. The form the thrust tailoff curve will take is a function of the time at which the command is given to terminate engine thrust, electrical-mechanical delays in the engine systems once the command to terminate engine thrust is given, and the thrust tailoff properties of the particular rocket engine. A typical engine thrust tailoff history is shown in figure 15.
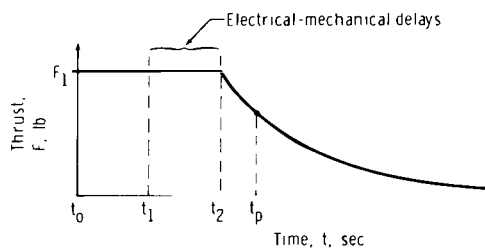

Figure 15. - Rocket engine thrust tailoff characteristics.

The landing procedure used for the LM is one where a commanded descent rate is given such that the vehicle approaches the landing site at a constant velocity. (In this situation, the rocket thrust is equal to the spacecraft weight.) At some preset height above the surface, the rocket engine thrust termination command is given. This time is represented by t_1 in figure 15. The station t_p on the time axis represents the position on the thrust curve when the footpad touches the surface.

The thrust curve in figure 15 is approximated in the range from t_o to t_2 by a constant F_1 and from t_2 to t by a polynominal or exponential function. The thrust force FTHRUST is given by the equation

$$\text{FTHRUST} = F_1 \qquad t_o < t < t_2 \tag{69}$$

46

and

$$\text{FTHRUST} = F_1 e^{-K\left(t-t_2\right)} + M_0 + M_1\left(t - t_2\right) + M_2\left(t - t_2\right)^2 + \ldots \quad t > t_2 \qquad (70)$$

where the constants F_1, K, M_0, M_1, et cetera are determined by fitting the appropriate function to empirically developed rocket engine thrust tailoff data.

If the location of the rocket engine on the spacecraft is such that the nozzle exit plane of the engine comes close to the landing surface while the engine is thrusting, an amplification in the engine thrust will occur. The thrust amplification is a complex function of such factors as surface geometry, rocket engine design, and engine-surface orientation. The amplification factor can be determined by experimental or, in some special cases, by analytical means. A typical amplification factor AMP variation with nozzle clearance for the LM descent-stage rocket engine thrusting near a flat surface is shown in figure 16. The plateau in the thrust amplification curve around zero nozzle clearance occurs when the rocket engine exit area is less than the throat area.
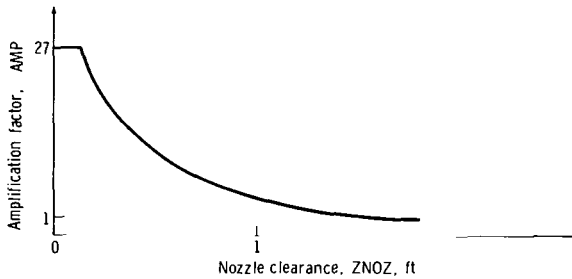

Figure 16. - Engine thrust amplification factor for the LM.

The total thrust on the vehicle is computed by establishing the distance of the centroid of the rocket engine nozzle exit plane above the surface (ZNOZ) and by determining the corresponding amplification factor by evaluating a function which describes the characteristics in figure 16. The amplification factor is then used to multiply the thrust force $\overrightarrow{\text{FTHRUST}}$ of equations (69) and (70) to obtain the total thrust TAF.

$$\overrightarrow{\text{TAF}} = \text{AMP} \left(\overrightarrow{\text{FTHRUST}}\right) \qquad (71)$$

The thrust force $\overrightarrow{\text{TAF}}$ is directed through the vehicle center of mass.

An additional force is involved if the nozzle of the descent-stage rocket engine contacts the landing surface. This force is due to the compressive failure forces of the rocket nozzle structure. The rocket nozzle structure is assumed to compress under constant load as the nozzle structure is forced onto the surface.

The forces produced on the vehicle because of nozzle crushing are distributed around the nozzle exit perimeter in proportion to the nozzle perimeter in contact with the landing surface. These forces are directed up the center line of the vehicle.

The total force vector $\overrightarrow{F_{TF}}$ due to the engine thrust and nozzle crushing load is

$$\overrightarrow{F}_{TF} = \overrightarrow{TAF} + \overrightarrow{FFL} \tag{72}$$

where $\overrightarrow{FFL}$ is the nozzle crushing load vector. These vectors are referenced to the body coordinate system. The moment vector $\overrightarrow{MTF}$ acting on the idealized vehicle because of the rocket thrust and nozzle crushing load is

$$\overrightarrow{MTF} = \vec{R}_{T} \times \overrightarrow{TAF} + \vec{R}_{F} \times \overrightarrow{FFL} \tag{73}$$

where the vector $\vec{R}_{T}$ is drawn from the origin of the body coordinate system to the centroid of the nozzle exit plane and where the vector $\vec{R}_{F}$ is drawn from the origin of the body coordinate to the centroid of the nozzle crushing load. The translational force vector $\overrightarrow{FTFI}$ (due to engine thrust and the nozzle crushing load) on the idealized vehicle in the inertial coordinate system is given by

$$\overrightarrow{FTFI} = \begin{bmatrix} T_{BI} \end{bmatrix} \vec{F}_{TF} \tag{74}$$

FORCES AND MOMENTS FROM REACTION CONTROL SYSTEMS

The forces and moments applied to a landing vehicle by the vehicle RCS are functions of the particular control system design. The equations used in this analysis for determining when control thrusters are activated are simplified approximations to the control logic used for the LM. Because of the large attitudes and attitude rates experienced by the landing vehicle during touchdown, the typical control thruster operation is for the thruster to be turned on and to remain on for a large portion of the time interval of interest. For this reason, the finer points of control system operation involving limit cycles, minimum jet on-time, and onboard computer sampling rates are not of prime importance in determining forces and moments applied to the vehicle. Consequently, relatively simplified control laws are used for landing dynamics simulation.

Three basic modes of control system operation are considered, including (1) attitude hold, (2) rate command, and (3) downward translation. The first two modes are basic modes used in the LM control system, and the third is a special landing mode which has been studied but has not been implemented for the LM.

It is assumed that the control system applies a positive or negative torque of fixed magnitude to the X_{B}-, Y_{B}-, or Z_{B}-axes, depending on the value of a linear

48

combination of attitude and attitude rate errors associated with the respective body axis. The attitude rate errors are computed from

$$\left. \begin{array}{l} E\omega_x = \omega_x - C\omega_x \\[2mm] E\omega_y = \omega_y - C\omega_y \\[2mm] E\omega_z = \omega_z - C\omega_z \end{array} \right\} \tag{75}$$

where $C\omega_x$, $C\omega_y$, and $C\omega_z$ are specified commanded attitude rates. The determination of attitude errors used in the simplified control laws involves treating attitude errors as components of a vector, so that deviations in the values of the Euler angles from the commanded values may be transformed into attitude errors which can be compared with body rate errors.

The commanded values for the Euler angles are specified by data input and are denoted by $C\theta_x$, $C\theta_y$, and $C\theta_z$. The deviations in Euler angles from the commanded values are computed from

$$\left. \begin{array}{l} D\theta_x = \theta_x - C\theta_x \\[2mm] D\theta_y = \theta_y - C\theta_y \\[2mm] D\theta_z = \theta_z - C\theta_z \end{array} \right\} \tag{76}$$

The deviations are assumed to be small. With this assumption, these deviations can be treated like components of a vector, so that they may be transformed by means of the transformation of equation (6) to corresponding attitude errors associated with the body system axes. The attitude errors for the body system axes are given by

$$\begin{bmatrix} E\theta_x \\ E\theta_y \\ E\theta_z \end{bmatrix} = \begin{bmatrix} T_{EB} \end{bmatrix} \begin{bmatrix} D\theta_x \\ D\theta_y \\ D\theta_z \end{bmatrix} \tag{77}$$

For the attitude-hold mode, the following error equations are evaluated.

$$\left.\begin{array}{l} EX = k_{11}E\theta_x + k_{12}E\omega_x \\[2mm] EY = k_{21}E\theta_y + k_{22}E\omega_y \\[2mm] EZ = k_{31}E\theta_z + k_{32}E\omega_z \end{array}\right\} \qquad (78)$$

where k_{11}, k_{12}, k_{21}, k_{22}, k_{31}, and k_{32} are constants, given by data input, which model a given control mode and where the commanded attitude rates are zero. The errors EX, EY, and EZ are compared to upper and lower bounds given by data input to determine if RCS thrusters should fire to produce a torque on the given axis. Let EXM, EYM, and EZM be positive numbers given by data input. The torque applied to the X_B-axis by RCS thrusters is determined from the following logic.

$$TRCSX = \left\{\begin{array}{ll} -TORQX & \text{if } EX > EXM \\[2mm] 0 & \text{if } -EXM < EX < EXM \\[2mm] +TORQX & \text{if } EX < -EXM \end{array}\right\} \qquad (79)$$

where TORQX is the magnitude of the torque which can be generated on the X_B-axis by the RCS thrusters. Similar logic is used to determine TRCSY and TRCSZ, the RCS torques about the Y_B- and Z_B-axes, respectively. The RCS torque vector is defined as

$$\overrightarrow{MRCS} = \begin{bmatrix} TRCSX \\ TRCSY \\ TRCSZ \end{bmatrix} \qquad (80)$$

The net force vector $\overrightarrow{FRCS}$ due to the RCS would be the null vector for this case.

The rate-command control mode is a special case of the attitude-hold mode where the attitude error bias is removed by setting k_{11}, k_{21}, and k_{31} equal to zero in equations (78) and where the commanded attitude rates are not necessarily zero. Appropriate bounds EXM, EYM, and EZM for attitude rate errors are specified, and the control logic of equation (79) is used to determine control torques.

The third control mode, downward translation, is more effective in preventing vehicle toppling during touchdown than either of the two modes discussed previously. The control logic consists of continuously firing those RCS thrusters which produce forces directed downward along the center line of the vehicle. In general, the vehicle would be flown in either of the two previously discussed modes for some specified time (approximately 1 second for lunar environment) after first contact with the surface; then, control would be switched to the downward translation mode. The delay in firing downward translation thrusters would avoid contributing to the effective weight of the vehicle during the period of maximum energy-absorption requirements on the landing gear.

The downward translation mode is simulated in the landing analysis by specifying a delay time from the instant of surface contact for initiation of the downward translation. During this delay period, control torques on the vehicle are computed according to either of the two previously discussed logics. After the delay period, no pure couple torques are applied to the vehicle by the control system, and a force of magnitude FRCSZ is applied vertically down the center line of the vehicle. The magnitude of FRCSZ is determined from the number of control jets available and from the thrust magnitude of each jet. The net force vector $\overrightarrow{FRCS}$ in the body coordinate system as a result of this landing mode is

$$\overrightarrow{FRCS} = \begin{bmatrix} 0 \\ 0 \\ -FRCSZ \end{bmatrix} \tag{81}$$

and then by transformation

$$\overrightarrow{FRCSI} = \begin{bmatrix} T_{BI} \end{bmatrix} \overrightarrow{FRCS} \tag{82}$$

where the vector $\overrightarrow{FRCSI}$ is the control jet force in the inertial coordinate system.

NET FORCE AND TORQUE VECTORS

The total force vector $\vec{F}$ (excluding gravity forces) acting on the idealized rigid-vehicle center of mass is the sum of individual external force vectors and is given by the equation

$$\vec{F} = \begin{bmatrix} FX \\ FY \\ FZ \end{bmatrix} = \overrightarrow{FCMG} + \overrightarrow{FTFI} + \overrightarrow{FRCSI} \qquad (83)$$

Similarly, the net torque on the idealized rigid-vehicle center of mass is given by the equation

$$\vec{T} = \begin{bmatrix} T_x \\ T_y \\ T_z \end{bmatrix} = \overrightarrow{TCMG} + \overrightarrow{MTF} + \overrightarrow{MRCS} \qquad (84)$$

The net vehicle forces FX, FY, and FZ and torques T_x, T_y, and T_z are used in conjunction with equations (10) to (12) and (13) to (15) to calculate the vehicle translational and rotational accelerations.

FORCES ON LANDING GEAR FOOTPADS

Description of Surface Models

It has been shown in the preceding sections that, given the position of each landing gear footpad in the body coordinate system, the instantaneous landing gear geometry and landing gear stroking forces can be determined. The position of each landing gear footpad is obtained by numerically integrating the equations of motion for each footpad. In the following paragraphs, the forces applied to the footpads by the landing surface are analyzed, and the equations of motion for the footpads are derived.

The mathematical surface models developed in this analysis are divided into two categories: (1) rigid surface models and (2) nonrigid surface models or soil models. A footpad that contacts a rigid surface model is capable only of sliding on the surface, and there is no footpad penetration into the surface. However, when a footpad contacts a nonrigid surface, the footpad penetrates the surface because of the plastic deformation

which the model is capable of simulating. For a given landing simulation, either type of landing surface can be specified for any footpad. Consequently, a wide variety of surface conditions can be modeled for a touchdown simulation.

For both surface models, the landing surface coincides with the X-Y plane of the inertial coordinate system. This plane is oriented with respect to the gravity vector by the transformation $\begin{bmatrix} T_{GI} \end{bmatrix}$ of equation (2), which uses an input slope value. Various holes and obstacles on the landing surface plane can be specified for each footpad in order to simulate a given surface topography. •Figure 17 defines the surface irregularity parameters $HOLE_n$ and $OBST_n$ which are specified for each footpad by data input.

The variable $HOLE_n$ denotes the surface elevation of each footpad at the point it first strikes the surface.
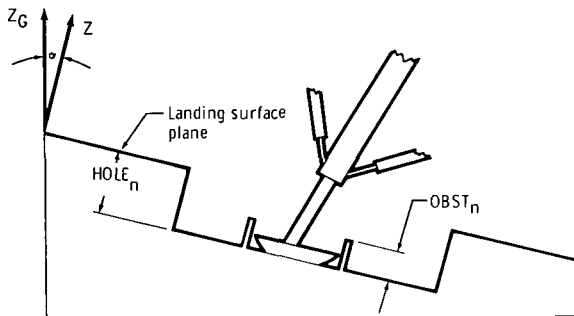
For the rigid surface model, several types of constraints for lateral motion of a footpad along the surface may be specified. A positive value for the input parameter $OBST_n$ in figure 17 denotes a complete lateral constraint on footpad motion. This constraint might be visualized as a vertical cylindrical wall with its height equal to $OBST_n$. Thus, after the footpad contacts the surface, it cannot move laterally until it rises above the wall. With this option, it is assumed that the footpad is rigid and that the sides of the wall produce a force equal and opposite to the strut forces resolved at the footpad. If a negative value of $OBST_n$ is selected, the footpad is allowed to slide on the surface under the influence of coulomb friction, with the friction coefficient specified by the variable U_n.

Figure 17. – Landing surface hole-obstacle definition.

Another type of constraint for sliding footpads are curbs which can be placed arbitrarily on the rigid surface. Two curbs may be specified for each footpad. The curb option is specified by using a positive value for the input parameter $CLUEW_n$. Normal forces between the pads and the curbs are developed by using a load-deflection table for the footpad. Forces parallel to the curbs are developed by a coefficient of friction UW_n and the normal force between the footpad and the curb. The direction of this frictional force is considered to be opposite to the sliding velocity of the footpad along the curb. Use of the curb option allows for simulation of crushable footpads, since a load-deflection table for footpad crushing normal to each curb is specified. When simulating landings where the footpads slide along the surface, the bottoms of the footpads are assumed to be rigid.

The nonrigid surface model is used to simulate landings on surfaces of various bearing strengths. Obstacle and curb options are omitted when this model is selected. The simulation of nonrigid models involves equations which are used to generate vertical

and lateral forces on a footpad as it translates into the soil. Various forms of these equations can be used, and they primarily reflect the variation of bearing strength with the position and velocity of a footpad. A detailed discussion of the various landing surface models and derivations of the footpad equations of motion are given in the following sections.

Rigid Surface Analysis

In the rigid surface model, there is no movement of a footpad in a direction normal to the surface when it is in contact with the surface. Therefore, there is no need for an equation of motion for footpad motion in the Z-direction. Likewise, if a footpad is completely constrained in lateral movement, no equations of motion are needed in the X- and Y-directions.

Since there is no equation of motion to be solved for vertical footpad motion, the vertical footpad position is determined through logic in the computer program. At each integration step, a tentative Z-position coordinate for each footpad is computed by assuming that the footpad is rigidly connected to the rigid-vehicle center of mass and by using landing gear geometry computed in the previous integration step. If this computation indicates that the footpad is beneath the local surface plane, the footpad is in surface contact and the Z-position coordinate is adjusted so that the footpad is on the local surface plane. If the computation reveals that the footpad is above the surface and if no previous surface contact has been made, then all footpad position coordinates and velocities are computed as though the footpad were rigidly connected to the vehicle. If the footpad is above the surface and if previous surface contact has been made, the Z-position coordinate is adjusted so that the footpad is back on the surface as long as compressive forces remain in the primary strut. (Placement of the footpad back on the surface effectively elongates the primary strut and thus unloads the honeycomb shock absorbers.) When all compressive forces in the primary strut have been relieved, the tentative Z-position coordinate of the footpad is used as the true footpad position. On simulations with lateral footpad constraints, the footpad is not completely free until the computed Z-position coordinate of the footpad indicates that the footpad is above the constraining obstacle. When the obstacles are cleared, footpad position and velocity are computed in the same manner as before surface contact by using newly deformed landing gear geometry.

As mentioned previously, the surface forces on a sliding footpad are determined from a coefficient of sliding friction and from forces generated between the footpad and a curb which it may contact. It is assumed that frictional forces on the bottom of a footpad occur in a direction opposite to the instantaneous sliding direction in the inertial X-Y plane, and this frictional drag force is computed by the equation

$$\overrightarrow{FDRAGP}_n = -\left(FZI_n\right)\left(U_n\right)\frac{\overrightarrow{\dot{SP}}_n}{\dot{SP}_n} \qquad (85)$$

54

where FZI_n = inertial Z-component of the vector $\overrightarrow{FPI}_n$ on the nth footpad (computed in eq. (67))

$\dot{\overrightarrow{SP}}_n$ = velocity vector of the nth footpad

U_n = coefficient of sliding friction between the nth footpad and the landing surface

   To determine the forces generated between a footpad and a curb, it is necessary to describe the lateral crushing characteristics of the footpad by data input. A typical crushing characteristic for a footpad is shown in figure 18.

   Curbs are oriented on the surface with respect to the initial footpad contact point. Two curbs can be designated for each footpad by the parameters shown in figure 19.
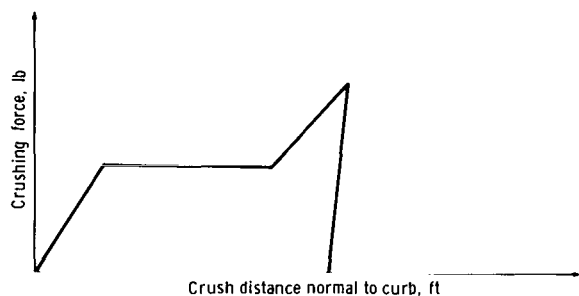

Figure 18. - Force-deflection diagram for footpad crushing.

   The inertial coordinates of a footpad are used to compute the distance from the center of the footpad to a curb at any time while the footpad is on the surface. If this distance is less than the original footpad radius, the amount of footpad crushing normal to the curb can be determined. The force between a footpad and a curb is then obtained from the footpad force-deflection diagram in figure 18.

   When a footpad first contacts the surface, the inertial position coordinates of the footpad are denoted by $[XPI_n, YPI_n, -HOLE_n]^T$. These coordinates are determined by transforming footpad coordinates in the body system to inertial coordinates. The coordinates
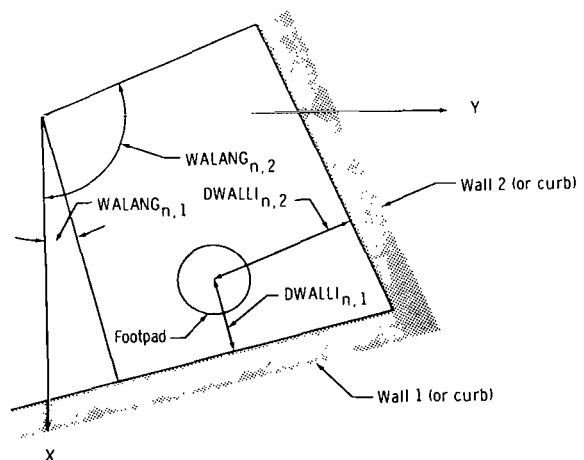
$DWALLI_{n,j}$ = the normal distance from n^{th} footpad center to j^{th} curb when footpad initially contacts the surface

$WALANG_{n,j}$ = the angle from the positive X-axis to a line in the X-Y plane normal to the jth curb of the nth footpad

Figure 19. - Schematic diagram of curb parameters on rigid surface.

of position vectors $\vec{W}_{n,j}$, which locate the intersection point of $DWALLI_{n,j}$ with a curb are computed from
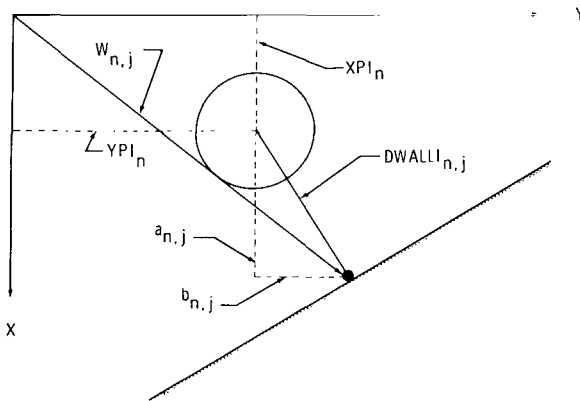
$$\vec{W}_{n,j} = \left[\left(XPI_n + a_{n,j} \right), \left(YPI_n + b_{n,j} \right), 0 \right]^T \tag{86}$$

where

$$a_{n,j} = DWALLI_{n,j} \cos \left(WALANG_{n,j} \right) \tag{87}$$

$$b_{n,j} = DWALLI_{n,j} \sin \left(WALANG_{n,j} \right) \tag{88}$$

Figure 20 illustrates a typical initial footpad-curb position.

Figure 20. - Initial footpad-curb position on rigid surface.

Consider a unit vector $\widehat{AI}_{n,j}$ which is normal to the curb and can be constructed by

$$\widehat{AI}_{n,j} = \frac{1}{DWALLI_{n,j}} \begin{bmatrix} a_{n,j} \\ b_{n,j} \\ 0 \end{bmatrix} \tag{89}$$

Then, a unit vector $\widehat{B}_{n,j}$ lying along the curb can be constructed by the vector cross product

$$\widehat{B}_{n,j} = \widehat{AI}_{n,j} \times \left[0, 0, 1 \right]^T \tag{90}$$

At any time after a footpad initially contacts the surface, vector $\vec{A}_{n,j}$ joining the footpad center with the point located by $\vec{W}_{n,j}$ can be constructed so that

$$\vec{A}_{n,j} = \begin{bmatrix} XPI_n + a_{n,j} - XP_n \\ YPI_n + b_{n,j} - YP_n \\ 0 \end{bmatrix} \tag{91}$$

where XP_n and YP_n are the instantaneous inertial coordinates for the footpad center. The current distance between the footpad center and the curb can then be computed from the vector dot product

$$\left. \begin{aligned} DWALL_{n,j} &= \vec{A}_{n,j} \cdot \hat{AI}_{n,j} \\ &= \frac{1}{DWALLI_{n,j}} \Big[\big(XPI_n + a_{n,j} - XP_n\big)\big(a_{n,j}\big) \\ &\quad + \big(YPI_n + b_{n,j} - YP_n\big)\big(b_{n,j}\big) \Big] \end{aligned} \right\} \tag{92}$$

Given the undeformed footpad radius PR, the variable $PSTRK_{n,j}$ is computed by

$$PSTRK_{n,j} = PR - DWALL_{n,j} \tag{93}$$

If $PSTRK_{n,j}$ is a negative quantity, the footpad is not in contact with a curb; but if $PSTRK_{n,j}$ is positive, its value represents the amount of footpad crushing normal to the jth curb. Appropriate logic is used to retain deformed footpad geometry for multiple impacts between footpads and curbs.

A crushing force value $PFRC_{n,j}$ is obtained from the footpad force-deflection diagram (fig. 18) by using $PSTRK_{n,j}$. Since $PFRC_{n,j}$ acts on the footpad in a direction normal to the curb, $PFRC_{n,j}$ can be written as the force vector

$$\vec{PFRC}_{n,j} = -\big(PFRC_{n,j}\big)\hat{AI}_{n,j} \tag{94}$$

57

Other forces on the footpads are generated at the curbs by friction between the footpad and curb. These frictional forces are computed from $PFRC_{n,j}$ and a coefficient of friction UW_n. Frictional forces are applied to the footpad parallel to the curb but opposite to the velocity of the footpad along the curb. A scalar product of $\overrightarrow{SP}$ and the unit vector $\widehat{B}_{n,j}$ along the curb is performed to obtain the proper sign for the friction force. The curb frictional force $\overrightarrow{FWF}_{n,j}$ on a footpad is then given by

$$\overrightarrow{FWF}_{n,j} = \pm \left(UW_n\right)\left(PFRC_{n,j}\right)\widehat{B}_{n,j} \tag{95}$$

It is assumed that the direction of $\overrightarrow{FWF}_{n,j}$ does not change during a numerical integration step.

All the instantaneous forces $\overrightarrow{FPI}_n$, $\overrightarrow{FDRAG}_n$, $\overrightarrow{PFRC}_n$, and $\overrightarrow{FWF}_n$ acting on a footpad are now accounted for, and the instantaneous vector equation of motion of a footpad is obtained from a vector sum of all forces acting on the footpad.

$$\ddot{\overrightarrow{SP}}_n = \left(\frac{\overrightarrow{FPI}_n + \overrightarrow{PFRC}_n + \overrightarrow{FWF}_n}{PMASS}\right) - \left(\frac{FDRAGP_n}{PMASS}\right)\frac{\dot{\overrightarrow{SP}}_n}{\dot{SP}_n} + \overrightarrow{G} \tag{96}$$

where PMASS = effective mass of a footpad

$\overrightarrow{G}$ = gravity vector in inertial coordinates

For computation purposes, equation (96) must be reduced to component form. Then, the equation becomes

$$\ddot{XP}_n = \frac{FXP_n}{PMASS} - \frac{FDRAGP_n\dot{XP}_n}{PMASS\sqrt{\left(\dot{XP}_n\right)^2 + \left(\dot{YP}_n\right)^2}} + g_x$$

$$\ddot{YP}_n = \frac{FYP_n}{PMASS} - \frac{FDRAGP_n\dot{YP}_n}{PMASS\sqrt{\left(\dot{XP}_n\right)^2 + \left(\dot{YP}_n\right)^2}} + g_y \tag{97}$$

$$\ddot{ZP}_n = 0$$

where

$$FXP_n = \left[\overrightarrow{FPI}_n + \overrightarrow{PFRC}_n + \overrightarrow{FWF}_n \right] \cdot [1, 0, 0]^T \qquad (98)$$

$$FYP_n = \left[\overrightarrow{FPI}_n + \overrightarrow{PFRC}_n + \overrightarrow{FWF}_n \right] \cdot [0, 1, 0]^T \qquad (99)$$

and g_x = component of gravity acceleration in the inertial system X-direction

g_y = component of gravity acceleration in the inertial system Y-direction

Equations (97) are integrated by a Runge-Kutta method, where FXP_n, FYP_n, and $FDRAGP_n$ have constant values over the integration interval. However, because of changes in footpad velocity components during the integration step, this method of solution does account for changes in direction of the drag force. Equations (97) have a singularity if the footpad velocity $\overrightarrow{SP}_n$ becomes zero. Since the equations are solved numerically over discrete time intervals, it is unlikely that the net result of any integration time step would yield a velocity value of exactly zero at the end of the interval. Instead, the numerical integration would actually change the direction of the velocity component. Such an occurrence would imply that the frictional force is capable of decelerating the footpad to zero velocity and then accelerating it in the opposite direction during the integration interval. Since in reality, a frictional force should not be able to accelerate a motionless footpad, the following special logic is used to avoid this problem.

If the sign of either $\dot{X}P_n$ or $\dot{Y}P_n$ is reversed during any integration step, it is assumed that the particular component of velocity is integrated to zero during the interval. The position of the footpad is then adjusted by determining an average velocity for the component during the integration interval. If the signs of both $\dot{X}P_n$ and $\dot{Y}P_n$ are changed during an integration time interval, then the footpad has stopped, and it is assumed that it remains at rest until the forces applied to it by the landing gear and the curbs are sufficient to overcome the friction force. The vector which represents the sum of the X- and Y-forces applied to the footpad by the landing gear and curbs is defined by

$$\overrightarrow{FXYP}_n = [FXP, FYP, 0]^T \qquad (100)$$

The magnitude of $\overrightarrow{FXYP}_n$ is compared with $FDRAGP_n$. Whenever $FXYP_n$ is larger than $FDRAGP_n$, one integration step is made, with X- and Y-components of $\overrightarrow{FDRAGP}_n$

determined by assuming $\overrightarrow{\text{FDRAGP}}_n$ acts in a direction opposite to $\overrightarrow{\text{FXYP}}_n$. After this integration step, nonzero values for $\dot{X}P_n$ and $\dot{Y}P_n$ are obtained, and equations (97) can again be used.

Numerical integration of the footpad equations of motion yields values for each footpad coordinate in the inertial system. These coordinates are transformed back into the body system, thus allowing for computation of new landing gear strut geometry and landing gear forces for the next integration interval.

Nonrigid Surface Analysis

The physics of the response of soil media to projectile impacts is not a well-developed science. Until recently, the best available knowledge of forces produced in soils could be obtained only from texts oriented to the study of building foundations (ref. 9). An interest in the ability of spacecraft to land on the lunar surface and speculation about the bearing properties of the lunar surface have fostered a considerable amount of research devoted to understanding the soil impact phenomena (refs. 6 and 10 to 12). Most of this research has been experimental, and only empirical methods of predicting forces which are applied to an impacting body by a soil medium have been developed. These methods generally attempt to relate soil forces on the impacting body with the penetration velocity of the body, along with the physical properties of the soil (such as density, relative density, cohesion, internal angle of friction, etc.). To gain some insight into the dynamic behavior of vehicles landing in various types of soils, mathematical soil models are useful.

Although several different mathematical soil models have been used in spacecraft landing simulations, only one of these models is discussed in this report. In this model, no attempt is made to relate the forces generated by the soil to the physical properties of the soil. Instead, the soil forces are related to footpad penetration and footpad velocity by constants, which represent penetration-resistance characteristics of the soil.

Forces in the inertial Z-direction, exerted on the footpad by the soil, are computed from an equation of the form

$$FZP_n = AP\left[K_1 + K_2\left(ZPEN_n\right) + K_3\left(\dot{Z}P_n\right) + K_4\left(\dot{Z}P_n\right)^2\right] \tag{101}$$

where AP = area of the bottom of a footpad

K_1 = bearing strength of the soil at the surface

K_2 = increase in soil bearing strength with depth

$ZPEN_n$ = penetration of a footpad in the inertial Z-direction

K_3 = increase in soil bearing strength with footpad velocity

K_4 = increase in soil bearing strength with the square of the footpad velocity

$\dot{ZP}_n$ = penetration velocity of a footpad

The forces applied to the footpad in the X-Y plane are obtained from a similar equation

$$\overrightarrow{FDRAG}_n = -APF\left[K_5 + K_6\left(SP_n\right) + K_7\left(ZPEN_n\right) + K_8\left(\dot{SP}_n\right)^2\right]\frac{\overrightarrow{\dot{SP}}_n}{\dot{SP}_n} \qquad (102)$$

where APF = frontal area of a footpad in contact with soil (assuming the footpad is cylindrically shaped, and computing area as a function of penetration)

K_5 = static soil resistance to horizontal movement

K_6 = increase in soil resistance to horizontal motion with respect to footpad lateral displacement

SP_n = lateral translation of a footpad

K_7 = increase in lateral resistance of the soil with respect to the depth of penetration of the footpad

K_8 = increase in soil resistance with respect to the square of the footpad horizontal velocity

$\overrightarrow{\dot{SP}}_n$ = instantaneous horizontal velocity of a footpad

By changing the constants in equations (101) and (102), numerous soil characteristics may be simulated. If lunar and planetary landings are to be studied, equations (101) and (102) can be as useful as some of the more complex soil impact models (ref. 6), since soil properties at a particular landing site will not be well defined and since it is desirable to simulate surface strength characteristics of a widely varying nature.

The equation of motion for inertial Z-translation of a footpad is obtained from the summation of forces in the Z-direction

$$\ddot{ZP}_n = \left(FZP_n - FZI_n\right)\frac{1}{PMASS} + g_z \qquad (103)$$

Equation (103) is solved numerically by assuming constant forces over an integration interval. The X and Y translation equations of motion are identical to equations (97), since $\overrightarrow{FDRAG}_n$ has the same form as $\overrightarrow{FDRAGP}_n$ in these equations.

61

A new variable $\overrightarrow{FGRND}_n$ is defined by

$$\overrightarrow{FGRND}_n = \overrightarrow{FDRAG}_n + \overrightarrow{FDRAGP}_n \tag{104}$$

and is substituted for $\overrightarrow{FDRAGP}_n$ in equations (97). This substitution allows for frictional forces on the underside of the footpads to be added to the soil forces of equation (102). Equations (97) are integrated in the same manner described previously.

STABILITY CRITERIA

A performance evaluation of a soft-landing system requires the simulation of many touchdown conditions. When a large number of touchdown simulations are required, the speed at which the computer can execute these simulations becomes a factor in the problem. In the evaluation of a soft-landing system for stability (tipover) performance, the computer running time can be reduced by defining stability criteria such that the computer can make the decision as to whether the landing being simulated will eventually be stable or unstable. Upon making this decision, the computer simulation is terminated.

A parameter representative of the state of stability of a particular landing is the magnitude of the minimum "stability distance." The stability distance is the shortest distance between the rigid-vehicle center of mass and a plane parallel to the gravity vector that passes through two adjacent landing gear footpads. This plane is defined as the "stability wall." Presented in f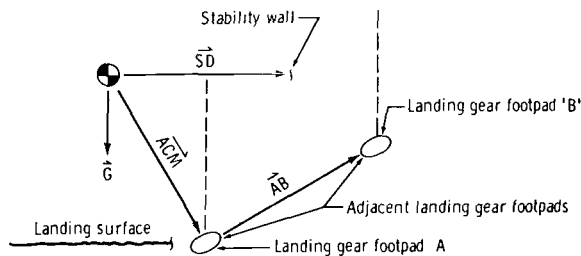igure 21 is the vector definition of the stability distance. The length of vector $\overrightarrow{SD}$ is the stability distance. The stability distance SD is calculated by the equation

$$SD = \frac{\overrightarrow{ACM} \cdot (\vec{G} \times \overrightarrow{AB})}{|\vec{G} \times \overrightarrow{AB}|} \tag{105}$$

Figure 21. - Vector definition of the stability distance.

where $\overrightarrow{AB}$ = vector connecting two adjacent landing gear footpads

$\overrightarrow{ACM}$ = vector connecting the rigid-vehicle center of mass and a landing gear footpad

$\vec{G}$ = gravity vector

The stability distance vector is calculated by the equation

$$\vec{SD} = \frac{SD(\vec{G} \times \overrightarrow{AB})}{\left|\vec{G} \times \overrightarrow{AB}\right|} \qquad (106)$$

A stability distance is computed in this manner for each stability wall.

If the rigid-vehicle center of mass is within an enclosure defined by stability walls passing through adjacent landing gear footpads, then the gravity action on the vehicle dynamics is stabilizing. (The center of mass and center of gravity are assumed to be coincident.) If the rigid-vehicle center of mass is outside of this enclosure, the gravity action on the vehicle dynamics is destabilizing, and the landing is declared unstable. If the vehicle is unstable, the degree of instability can be gaged by the magnitude of the "overturning velocity" at the instant the rigid-vehicle center of mass passes through the stability wall. The overturning velocity V_o is calculated by the equation

$$V_o = \vec{V} \cdot \hat{SD} \qquad (107)$$

where $\vec{V}$ is the translational velocity vector of the rigid-vehicle center of mass.

Also, instantaneous values of the stability distance, overturning velocity, and vehicle kinetic energy can be used in determining if the landing will eventually be stable. At the instant a landing gear footpad contacts the landing surface, the vehicle has a given kinetic energy. Subsequent motion will increase or decrease the initial vehicle kinetic energy, depending on the amount of energy dissipated by the landing gear system or the energy gain due to the lowering of the rigid-vehicle center of mass. When the vehicle kinetic energy has been dissipated to the point that it is less than approximately 10 percent of the initial vehicle kinetic energy at touchdown, the landing gear struts have usually undergone maximum stroking. After maximum stroking of the landing gear struts occurs, the resulting vehicle motion will generally be rigid-body rotation about two adjacent landing gear footpads on the landing surface. After computing the minimum stability distance to each stability wall, a landing can be declared stable if it satisfies the following conditions:

1. The vehicle kinetic energy is less than 10 percent of the initial touchdown kinetic energy. (This constraint can be replaced by not declaring a landing to be stable until landing gear struts have completed stroking.)

2. The rigid-vehicle center of mass is inside the stability walls.

3. The two adjacent landing gear footpads for which the minimum stability distance is computed are on the landing surface.

4. The rigid-vehicle center of mass is moving away from the stability wall with some preselected minimum velocity.

An index of the degree to which the landing was stable can be judged by the magnitude of the minimum stability distance obtained during the landing.

The capability of the computer program to decide whether a landing is stable or unstable enables the program to be operated in a mode where a "stability boundary" can be defined with a minimum number of landing simulations. The stability boundary is a curve of vertical touchdown velocity V_v compared to horizontal touchdown velocity V_h; this curve separates the V_v-V_h plane into regions of velocity conditions that result in either stable or unstable landings. The generation of the stability boundary is accomplished through program logic, which enables the program to choose touchdown velocity conditions to be simulated, based on the stability results of previous landing simulations in the same computer run. This capability is of considerable importance when extensive studies of landing stability performance are required.

ANALYTICAL-EXPERIMENTAL DATA CORRELATION

The degree to which the mathematical model of a soft-landing system represents physical reality depends primarily upon the assumptions made in the analysis. In evaluating landing performance of a soft-landing system, factors such as vehicle stability and landing gear energy-absorption characteristics are of prime importance. In light of the complexities of a soft-landing system, some approximations are inevitable, and for this reason, experimental verification of the analysis is desirable.

Several experimental programs have been conducted to develop landing dynamics data. Various LM models have been drop tested at the Langley Research Center, at MSC, and at NASA contractor facilities. References 13 to 15 present some of the data from these test programs. Reference 15 contains comparisons of experimental results of full-scale LM drop tests and theoretical predictions of the mathematical analysis presented in this report.

The analytical-experimental data correlation presented in this report is restricted to landing dynamics simulations of a 1/6-scale LM model. The experimental data were developed by a NASA contractor (ref. 13) by dropping a 1/6-scale LM model on a plywood surface (fig. 22). Critical stability and landing gear energy-absorption data were obtained by varying the model touchdown conditions.

The forces acting on the 1/6-scale model during landing are gravity forces and landing gear strut forces. The landing gear strut forces are due to friction and to the deformation of the honeycomb cartridges housed inside the struts. The landing gear footpads are spikes that penetrate into the plywood landing surface and constrain the footpad from lateral motion during impact. The effects of the landing gear footpad penetration into the landing surface on the model touchdown dynamics are accounted for by modifying the primary strut load-stroke diagram.

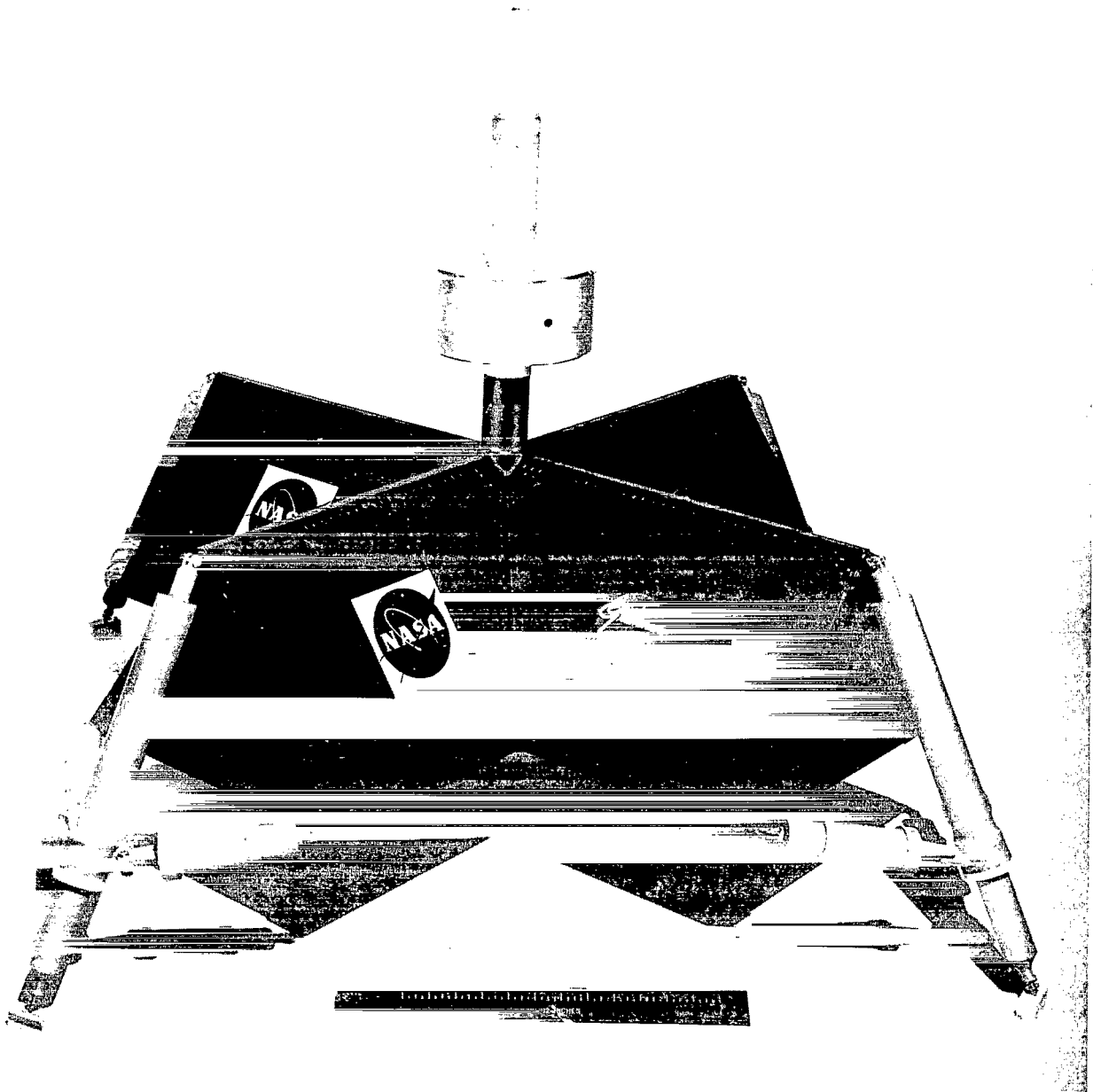A schematic drawing of the 1/6-scale LM model is presented in figure 23. Landing gear strut load-stroke diagrams are presented in figure 24.
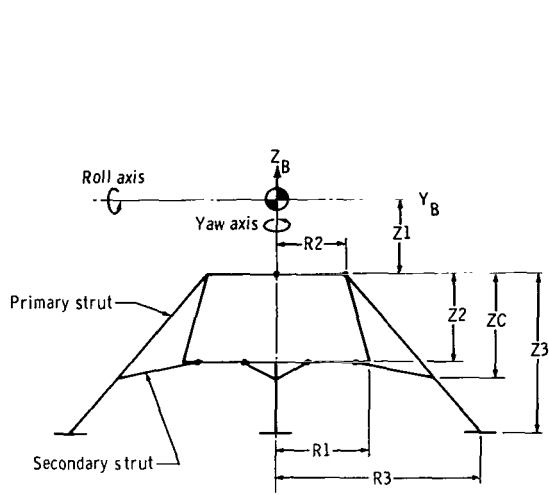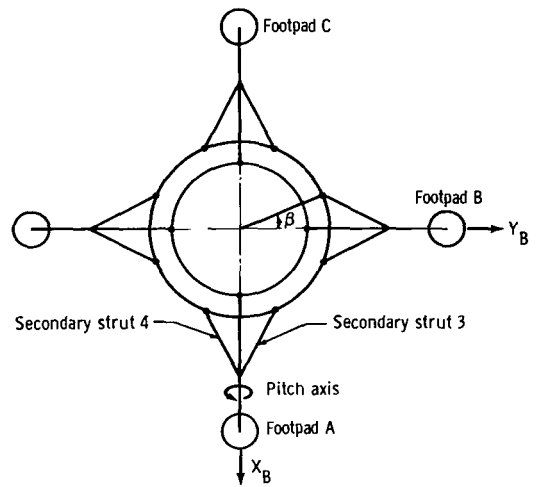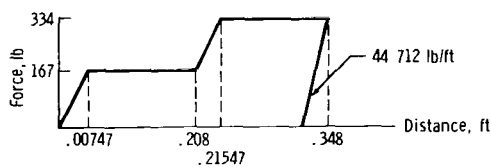
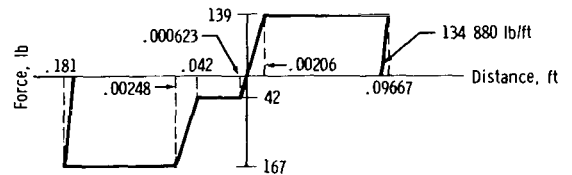Figure 22. - The 1/6-scale LM model.
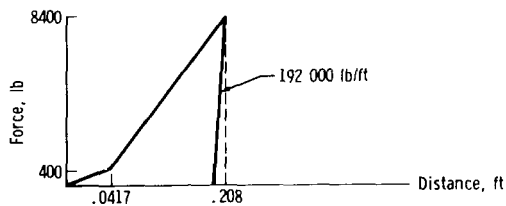
(a) Side view.

(b) Top view.

Figure 23. - The 1/6-scale LM model geometry.

(a) Primary strut load-stroke diagram for a 1/6-scale LM model.

(b) Secondary strut load-stroke diagram for a 1/6-scale LM model.

(c) Landing surface load-deformation characteristics.

Figure 24. - Model physical characteristics.

The geometric parameters and surface deformation properties for the model are as follows:

R1 = 1.639 ft   Z1 = 0.490 ft
R2 = 1.562 ft   Z2 = 0.806 ft
R3 = 2.221 ft   Z3 = 1.351 ft
β = 19.72°   ZC = 0.952 ft
I_{zz} = 0.994 slug-ft^2

I_{xx}, I_{yy} = 1.397 slug-ft^2

I_{xy}, I_{xz}, I_{yz} = 0 slug-ft^2

Bearing friction coefficient μ_B = 0.10
Bearing overlap = 0.396 ft

Two model touchdown orientations were tested and simulated. These touchdown orientations resulted in planar motion of the model. One orientation is the planar 2-2 landing mode. This type of landing occurs when the two trailing landing gear footpads strike the surface simultaneously, followed by the simultaneous impact of the two leading footpads.

The second orientation is the planar 1-2-1 landing mode. This type of landing occurs when the trailing landing gear footpad contacts the landing surface and is followed either by simultaneous contact of the two midgear footpads or by contact of the leading footpad. The 2-2 landings pose critical problems for stability and for secondary strut compression stroking. The 1-2-1 landings present critical primary strut compression stroke-out problems.

Figure 25 shows a comparison of the analytically predicted and the experimentally measured model vertical acceleration during the first 0.16 second of a landing. The 1/6-scale LM model was oriented such that a planar 2-2 landing occurred. After the first 0.12 second of the landing, the resulting motion of the model is rigid-body rotation about the two downhill landing gear footpads. The model was initially pitched up 5° with respect to the horizontal, with horizontal velocity in the downhill direction. The landing surface was sloped 5°, with 4-inch depressions superimposed on the slope under the downhill landing gear footpads.
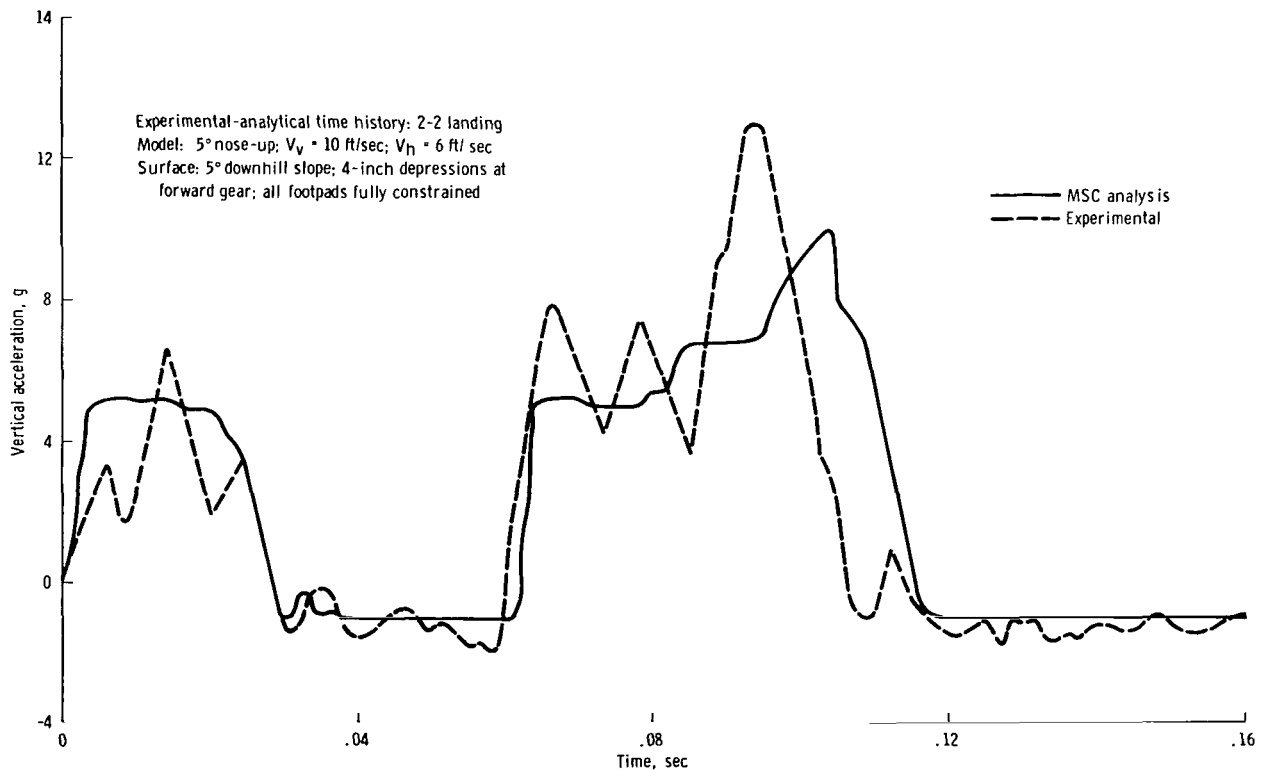

Figure 25. - Analytical-experimental correlations of the vertical acceleration of a 1/6-scale LM model.

The major difference between the analytical and experimental time histories shown in figure 25 is the spiked oscillation of the experimental curve. The cause of this phenomenon has not been established, but a likely reason may be that excessive binding of the primary strut inner cylinder occurred during stroking. Some binding is expected and is accounted for in the analysis by bearing friction forces. However, a constant bearing friction coefficient is assumed, and possible deviations from this idealization could occur if manufacturing tolerances of the model landing gear are not equivalent to prototype hardware. Some wearing of the bearing surface could also occur after several drops in the drop-test series.

The following explanation of the various features of the acceleration time history in figure 25 is made with reference to the analytical curve. The first acceleration pulse shown in figure 25 is due to the initial impact of the trailing landing gear footpads. Subsequent model rotational and translational motion brings the downhill landing gear footpads in contact with the surface, which produces the second acceleration pulse. After the first acceleration pulse, the model goes into a free-flight period of approximately 0.02 second. The first acceleration pulse is produced predominantly by the first-stage honeycomb-crushing forces in the trailing landing gear primary struts. The second acceleration pulse is predominantly due to the primary strut loads of the downhill landing gears. The first plateau of the second acceleration pulse is mainly due to the first-stage honeycomb-crushing force of the primary strut. The second plateau in the second acceleration pulse is due to the secondary strut forces acting on the primary strut, producing an increase in the primary strut bearing friction force. The final peak in the acceleration pulse is due to the primary strut stroking into the second stage of the honeycomb shock absorber. In this case, the primary struts stroked a distance of 0.01 foot into the second-stage honeycomb shock absorber. Shown in figure 26 is a comparison of analytical and experimental model pitch rates for the same landing. The
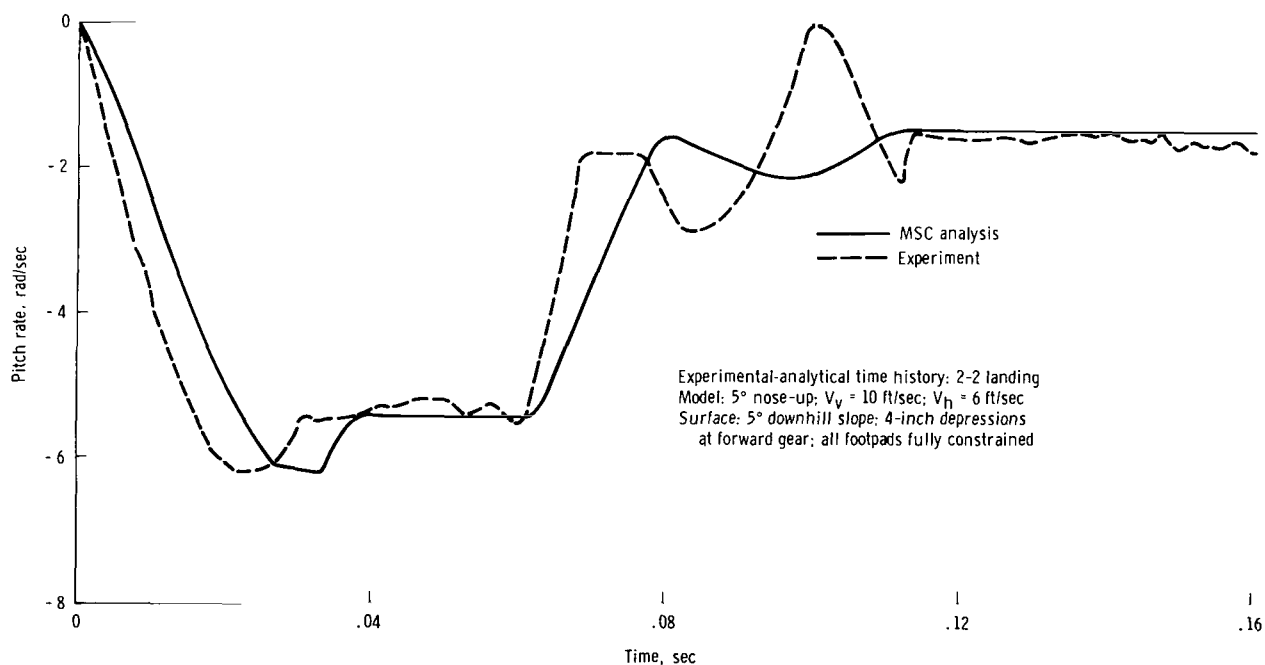

Figure 26. - Analytical-experimental pitch rate correlation of a 1/6-scale LM model.

68

initial rise in pitch rate is predominantly due to the forces of the trailing landing gear primary struts. As the model rotates, the vertical forces are diminished to the point that the lateral constraining forces produce a positive pitching acceleration before the model goes into the period of free flight. At approximately 0.06 second, the downhill landing gear footpads strike the landing surface. The resulting forces reduce the pitch rate from -5.5 rad/sec to -2.0 rad/sec. After 0.12 second, the model has experienced maximum stroking in the landing gear struts, with the resulting motion being near-rigid-body rotation about the two forward footpads.

The model drop-test data used in the detailed correlation shown in figures 25 and 26 were the only detailed time-history data available from this particular model test series, and the data were not selected because they represented the best analytical-experimental correlation. In fact, these data probably represent one of the poorest correlations expected, since the model did not overturn in the test, while the computer-simulated landing did overturn. As shown in figure 27, the computer program correctly predicted stability results for the other model drops in the test series. The touchdown attitudes, surface slope, and surface depressions for the test results in figure 27 are the same as those of the drop-test data in figures 25 and 26.
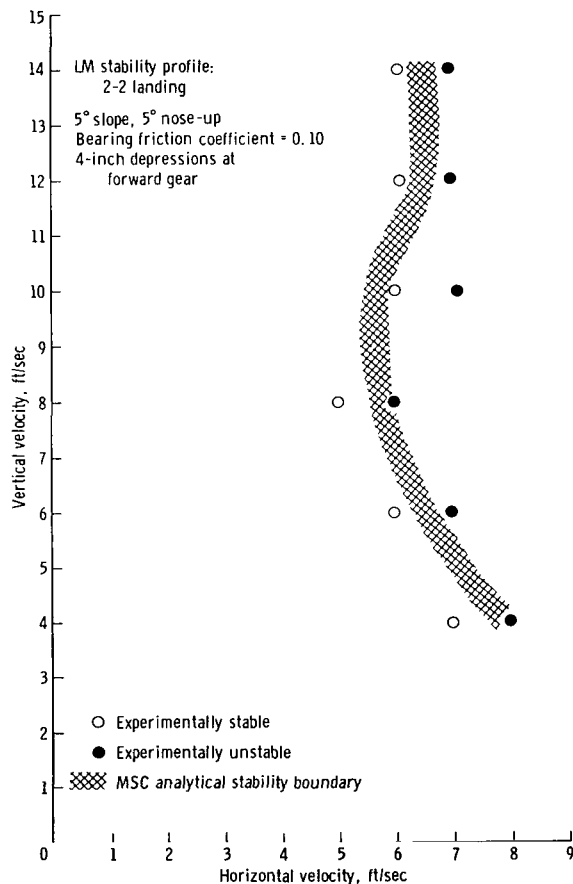
The predicted stability boundary is within 1 ft/sec of the experimental boundary at the vertical touchdown velocity of 10 ft/sec. For other values of vertical velocity, the analytical profile is within the bounds of the experimental profile. The overall correlation between analytical and experimental stability results seems good. The data indicate that the stability profiles for an LM-type landing gear system can be computed to within 1 ft/sec for landings on rigid surfaces with fully constrained landing gear footpads. Correlations of computer simulations and drop tests for maximum primary and secondary compression strokes are presented in table I.

The overall correlation between the predicted and the measured parameters of the 1/6-scale LM model landings was good because the load-stroke properties of the landing gear struts and the landing surface force-deformation properties were well defined. If the same degree of definition can be obtained for a full-scale landing vehicle, the predicted landing performance would have comparable accuracy.

Figure 27.- Analytical-experimental stability correlation of a 1/6-scale LM model.

TABLE I. - CORRELATION OF ANALYTICAL AND EXPERIMENTAL

LANDING GEAR STRUT STROKE DATA

Landing (a)	Touchdown velocity, ft/sec		Amount of stroke, in.	
	V_v	V_h	Experimental data	Analytical data
Primary strut				
1-2-1	-5.0	7.0	3.81	3.934
1-2-1	-7.0	6.2	3.88	4.264
1-2-1	-10.0	4.0	4.07	4.050
1-2-1	-13.0	1.2	3.91	3.988
Secondary strut				
2-2	-4.0	7.0	1.16	1.007
2-2	-6.0	8.0	1.86	1.804
2-2	-8.0	6.0	2.33	2.358
2-2	-10.0	6.0	2.72	2.771

[a]1-2-1 landing: 5° nose-up; downhill landing; 5° surface slope; 4-inch depressions under midgear and downhill gears. 2-2 landing: 5° nose-down; uphill landing; 5° surface slope; 4-inch depressions under trailing gears.

CONCLUDING REMARKS

The equations governing the touchdown dynamics of a soft-landing spacecraft have been derived and presented. A digital computer simulation based on these equations has been developed. The computer program has been utilized successfully in the development of the Apollo lunar module landing gear system and for predicting the lunar landing performance of the lunar module.

The accuracy of the computer simulation of the lunar module landing was established through correlation with data measured during tests of a dynamically scaled model. Comparison of data indicates that touchdown velocities which result in spacecraft overturning can be predicted to within 1 ft/sec. Landing gear strut stroking can be predicted to within 10 percent, provided significant stroking occurs.

Theoretical methods have proved to be satisfactory for guiding landing gear system development and for determining spacecraft landing performance. This fact, coupled with the problems associated with providing an adequate test environment, will undoubtedly result in more emphasis being placed on theoretical procedures, such as the ones presented in this paper, for future spacecraft landing system development.

Manned Spacecraft Center
National Aeronautics and Space Administration
Houston, Texas, September 4, 1970
914-50-20-89-72

APPENDIX

PROPELLANT SLOSHING

It is likely that future spacecraft with a soft-landing capability, like the Apollo LM, will use liquid propellants in their primary propulsion systems. During the descent and subsequent touchdown of the spacecraft, liquid propellant is consumed, resulting in partially filled propellant tanks at the instant of touchdown. Upon initial spacecraft contact with the landing surface, the residue propellant is subjected to a sloshing phenomenon which influences the touchdown performance of the spacecraft landing system.

The mathematical model used to simulate the propellant sloshing during the spacecraft touchdown is based on "linear sloshing theory" (refs. 16 and 17). Linear sloshing theory is used to compute the sloshing force on the side of the propellant tank. If the assumption is made that the sloshing force on the tank walls is due to the first sloshing mode (as defined in refs. 16 and 17 and fig. 28) and that the higher sloshing modes are negligible, then the sloshing forces can be calculated by
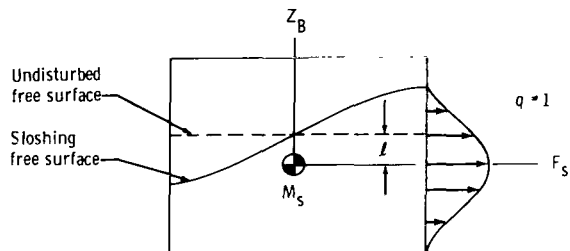
$$F_w = F_s \ddot{Z}_B q \qquad (108)$$

Figure 28. - Sloshing force distribution on propellant tank wall (first sloshing mode).

where F_w = total force applied to the tank wall by the sloshing propellant, lb

F_s = force per unit vertical tank acceleration caused by unit sloshing amplitude, $(lb/ft)/(ft/sec^2)$

q = sloshing amplitude, ft

$\ddot{Z}_B$ = vertical acceleration of the propellant tank in the body coordinate system, ft/sec^2

The force F_s is determined from linear sloshing theory (ref. 18) by integrating the force distribution on the propellant tank wall due to a unit sloshing amplitude. Figure 28 illustrates a typical sloshing force distribution on the tank wall. The force F_s is located at the centroid of the force distribution, a distance ℓ below the undisturbed free surface level.

The equation which governs the sloshing amplitude is given by

$$\ddot{q} = -\ddot{q}_B - \omega^2 \ddot{Z}_B q \qquad (109)$$

where $\ddot{q}_B$ = rigid-vehicle acceleration of the propellant tank normal to the vertical axis of the tank, ft/sec^2

ω^2 = sloshing frequency squared per unit vertical tank acceleration (rad/sec)^2/(ft/sec^2)

$\ddot{Z}_B$ = vertical acceleration of the propellant tank

The frequency term ω is determined from linear sloshing theory (ref. 18) and is a function of such factors as propellant tank shape, propellant loading, and gravity field. Numerical integration of equation (109) gives the sloshing velocity and amplitude-time histories which are used in equation (108) to calculate F_w.

When a partially filled propellant tank is subjected to a constant lateral acceleration, the inertial resistance of the sloshing propellant is reflected as a force on the side of the propellant tank. Consider the residue propellant mass as being comprised of a fixed mass M_f and a sloshing mass M_s. When residue propellant mass is considered to be two masses, a linear spring-mass system can be constructed which is analogous to the sloshing dynamics.

In the linear spring-mass system, the force on the propellant tank wall as a result of sloshing is

$$F_w = M_s \omega_n^2 q \qquad (110)$$

where M_s = sloshing mass, slugs

ω_n = natural sloshing frequency, rad/sec

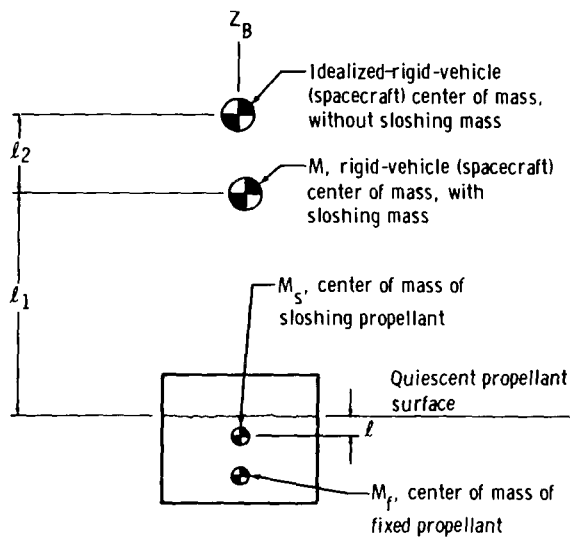By equating equations (108) and (110) and by noting that $\omega_n^2 = \omega^2 \ddot{Z}_B$, then

$$F_s \ddot{Z}_B \vec{q} = M_s \omega^2 \ddot{Z}_B \vec{q} \qquad (111)$$

73

and

$$M_s = \frac{F_s}{\omega^2}$$ (112)

Once the sloshing mass is determined, modifications to the total spacecraft mass characteristics must be made in order to account for the separation of the sloshing mass from the remaining vehicle mass.

Figure 29 illustrates the location of the propellant masses and the rigid-vehicle center of mass, with and without propellant sloshing mass. The propellant tank is assumed to be symmetric about the Z_B-axis. The center of mass of the sloshing propellant M_s is distance ℓ below the quiescent propellant surface, as is the centroid of the sloshing force F_w. By taking moments about the center of mass of the rigid vehicle with sloshing propellant, ℓ_2 is obtained from

$$\ell_2 = \frac{M_s}{M - M_s}\left(\ell_1 + \ell\right)$$ (113)

where M is the total mass of the spacecraft, including the propellant mass.

At this point, the idealized rigid spacecraft is considered to be a two-mass system; the two independent masses are the mass of the rigid vehicle excluding the sloshing mass $(M - M_s)$ and the sloshing mass itself. The influence of one mass on the other is the propellant sloshing force. Mass characteristics for landing vehicles are most often available in a form which assumes the propellant to be a rigid part of the spacecraft. To properly incorporate this type of data into landing dynamics simulations which consider propellant sloshing, the mass data require some modification.

Modification of the vehicle mass moments of inertia involves only those mass moments about the X_B- and Y_B-axes, because the sloshing mass is allowed essentially two degrees of freedom (motion in the X_B-Y_B plane). The change in the mass

Figure 29. - Influence of sloshing propellant on the rigid-vehicle center of mass.

moment of inertia about the Z_B-axis is assumed negligible because of small-amplitude displacements. The following equation gives the new mass moments of inertia for a rigid spacecraft, corrected for removal of the sloshing mass.

$$\left.\begin{array}{l} I_{xx,f} = I_{xx} - \left(M - M_s\right)\ell_2{}^2 - M_s\left(\ell_1 + \ell\right)^2 \\[2ex] I_{yy,f} = I_{yy} - \left(M - M_s\right)\ell_2{}^2 - M_s\left(\ell_1 + \ell\right)^2 \\[2ex] I_{zz,f} = I_{zz} \end{array}\right\} \qquad (114)$$

where $I_{xx,f}, I_{yy,f}, I_{zz,f}$ = modified mass moments of inertia in the body system of the rigid vehicle with the sloshing mass excluded

I_{xx}, I_{yy}, I_{zz} = mass moments of inertia in the body system of the rigid vehicle, including the total residue propellant mass

The sloshing force vector $\vec{F}_w$, which is the interacting force between $(M - M_s)$ and M_s, has body system components given by

$$\vec{F}_w = \begin{bmatrix} F_{PB,x} \\[1.5ex] F_{PB,y} \\[1.5ex] 0 \end{bmatrix} \qquad (115)$$

The body system components are transformed into inertial coordinate system components by

$$\begin{bmatrix} F_{B,x} \\[1.5ex] F_{B,y} \\[1.5ex] F_{B,z} \end{bmatrix} = \begin{bmatrix} T_{BI} \end{bmatrix} \begin{bmatrix} F_{PB,x} \\[1.5ex] F_{PB,y} \\[1.5ex] 0 \end{bmatrix} \qquad (116)$$

where $[T_{BI}]$ = transformation matrix given by equation (3)

$F_{B,x}, F_{B,y}, F_{B,z}$ = sloshing force components in the inertial coordinate system

The sloshing forces create torques about the center of mass of the idealized rigid vehicle. The torques $T_{f,x}$ and $T_{f,y}$ about the X_B- and Y_B-axes are calculated from

$$
\left. \begin{array}{l} T_{f,x} \approx F_{BP,y} \left(\ell_1 + \ell_2 + \ell \right) \\[2ex] T_{f,y} \approx F_{BP,x} \left(\ell_1 + \ell_2 + \ell \right) \end{array} \right\} \tag{117}
$$

The sloshing forces and torques are considered to be external forcing functions in the solutions of the rigid-vehicle equations of motion.

REFERENCES

1. Mantus, M.; Lerner E.; and Elkins W.: Landing Dynamics of the Lunar Excursion Module (Method of Analysis). Rept. LED-520-6, Grumman Aircraft Engineering Corp., March 6, 1964.

2. Doiron, Harold H.: Lunar Landing Dynamics Studies. Paper presented at Eleventh Manned Spacecraft Center Technical Symposium, Houston, Texas, Jan. 25, 1965, pp. 1-19.

3. Walton, W. C., Jr.; Herr, R. W.; and Leonard, H. W.: Studies of Touchdown Stability for Lunar Landing Vehicles. J. Spacecraft Rockets, vol. 1, no. 5, Sept.-Oct. 1964, pp. 552-556.

4. Walton, William C., Jr.; and Durling, Barbara J.: A Procedure for Computing the Motion of a Lunar-Landing Vehicle During the Landing Impact. NASA TN D-4216, Oct. 1967.

5. Graves, Donald L.: A Program to Derive Analytical Model Representations of the Apollo Spacecraft and Its Launch Vehicles, Apollo Lunar Landing Analysis (ALLA) Computer Program Users Manual, Final Report. Rept. D2-84125-13, The Boeing Co., May 1967.

6. Anon.: Lunar Module (LM) Soil Mechanics Study. Final Report. Rept. AM-68-1, Energy Controls Division, Bendix Corporation, May 1, 1968.

7. Holder, Ben Walton: A Study of the Effect of Landing Gear Mass and Inertia on Spacecraft Touchdown Stability. M.S. Thesis, Univ. of California, Los Angeles, 1966.

8. Thomson, William Terrell: Introduction to Space Dynamics. John Wiley and Sons, Inc., 1963.

9. Terzaghi, Karl: Theoretical Soil Mechanics. John Wiley and Sons, Inc., 1943.

10. Halajian, J. D.; Reichman, J.; and Karafiath, L. L.: Correlation of Mechanical and Thermal Properties of Extraterrestrial Materials. NASA CR-83895, Jan. 1967.

11. Nelson, J. D.; and Vey, E.: Bearing Capacity of Lunar Soil. Paper presented at the American Society of Mechanical Engineers Winter Annual Meeting, New York, New York, Nov. 29-Dec. 4, 1964, Paper no. 64-WA/AV/13.

12. Scott, Ronald F.: Principles of Soil Mechanics. Addison-Wesley Publishing Co., Inc., (Reading, Mass.), 1963.

13. Cary, John W.: Landing Dynamics of the Lunar Excursion Module (1/6 Scale Model III, Test-Analysis Correlation). Rept. LED-520-12, Grumman Aircraft Engineering Corp., May 16, 1966.

14. Herr, Robert W.; and Leonard, H. Wayne: Dynamic Model Investigation of Touchdown Stability of Lunar-Landing Vehicles. NASA TN D-4215, Oct. 1967.

15. Blanchard, Ulysse J.: Full-Scale Dynamic Landing-Impact Investigation of a Prototype Lunar Module Landing Gear. NASA TN D-5029, Mar. 1969.

16. Abramson, H. Norman, ed.: The Dynamic Behavior of Liquid in Moving Containers with Applications to Space Vehicle Technology. NASA SP-106, 1966.

17. Lomen, D. O.: Liquid Propellant Sloshing in Mobile Tanks of Arbitrary Shape. NASA CR-222, Apr. 1965.

18. Lomen, D. O.: Digital Analysis of Liquid Propellant Sloshing in Mobile Tanks with Rotational Symmetry. NASA CR-230, May 1965.